Chemical Science

ROYAL SOCIETY OF CHEMISTRY

REVIEW

View Article Online
View Journal | View Issue

Cite this: *Chem. Sci.*, 2025, **16**, 22852

Lattice-coherent interface-reinforced sodium-layered oxide cathodes

Sun-Qi Su,†[ab] Qi-Cong Ling,†[ab] Yan-Jiang Li,*[bc] Ya-Ping Yan,*[d] Yan-Fang Zhu*[ab] and Yao Xiao *[ab]

Sodium-layered transition metal oxide (Na_xTMO_2) is recognized as a promising cathode material for high energy density sodium ion batteries (SIBs). Nevertheless, its practical implementation is hindered by persistent issues such as structural degradation, sluggish Na^+ diffusion kinetics, and air sensitivity. To counteract these drawbacks, a lattice-coherent interface is employed to reform Na_xTMO_2. Herein, recent progress related to the construction of lattice-coherent interfaces in Na_xTMO_2 cathodes is summarized in this review, including bi-phase and tri-phase heterostructures. The constraining of interlayer sliding and phase structure degradation as a result of the high thermodynamic energy barrier originating from the lattice-coherent interface is comprehensively analyzed. The ion transport kinetics and moisture stability of Na_xTMO_2 with regard to the lattice-coherent interface are also disscussed in depth. The relationships between the interface interlocking heterostructure in the lattice and electrochemical performance are elucidated. To explore the lattice-coherent configuration, we emphasized AI and state-of-the-art *in situ* characterization techniques during the design and construction of Na_xTMO_2 cathodes. These insights are expected to establish a new design paradigm for high-performance layered cathode materials for SIBs.

Received 25th September 2025
Accepted 31st October 2025

DOI: 10.1039/d5sc07446k

rsc.li/chemical-science

1 Introduction

The global energy transition, driven by fossil fuel depletion and the dual-carbon strategy, relies on advanced electrochemical energy storage. However, the dominant lithium-ion batteries (LIBs) are constrained by scarce lithium resources.[1–4] As depicted in Fig. 1a, lithium accounts for only 20 mg L^{-1} in the Earth's crust, and the reserves are highly concentrated in specific regions of Chile, Argentina, and Australia, which account for approximately 80% of the total reserves. Such geographical disparity will inevitably result in price volatility and vulnerable supply chains.[5–9] With the high crustal abundance (23 600 mg L^{-1}) and uniform distribution of sodium resources, SIBs present promising application prospects for the future. Furthermore, the cost of SIBs is also 30–40% lower than that of LIBs (Fig. 1b).[10–14]

Because of these advantages, SIBs are promising alternatives for energy storage. Compared with LIBs, SIBs are more suitable for equipment with low energy density requirements, such as grid scale energy storage and low-speed electric vehicles.[15–19] Accordingly, high-performance cathode materials are desirable for practical applications of SIBs. Currently, cathode materials for SIBs are generally classified into three major categories: polyanionic compounds, Prussian blue analogues (PBAs), and Na_xTMO_2.[20–24] The polyanionic compounds present exceptional thermal stability and long cycle life, yet their practical applications are hindered by intrinsically low electronic conductivity, limited specific capacity, and low redox potential.[25–29] PBAs achieve ultra-high rate performance through open frameworks, but are unstable due to crystalline water-induced side reactions. The Na_xTMO_2 emerge as promising cathodes because they combine high capacity, suitable voltage, and compatibility with existing production methods.[30–32]

Typically, the crystal structure of Na_xTMO_2 features alternative stacking of Na^+ layers and transition metal oxide (TMO_2) slabs along the *c*-axis. In this configuration, the TM^{n+} ions occupy octahedral sites within the TMO_2 layers, coordinated by oxygen atoms, while Na^+ ions reside in either octahedral or trigonal prismatic interlayer sites.[33–37] The particular polymorph observed in Na_xTMO_2 is dictated by the arrangement of the oxygen layer and the local coordination geometry of Na^+.

[a]*College of Chemistry and Materials Engineering, Wenzhou University, Wenzhou 325035, China. E-mail: yanfangzhu@wzu.edu.cn; xiaoyao@wzu.edu.cn*

[b]*Zhejiang Provincial Key Laboratory of Advanced Battery Materials and Technology, Wenzhou University Technology Innovation Institute for Carbon Neutralization, Wenzhou 325035, China*

[c]*Key Laboratory of Spin Electron and Nanomaterials of Anhui Higher Education Institutes, Suzhou University, Suzhou 234000, China. E-mail: yjli@ahszu.edu.cn*

[d]*Henan Engineering Technology Research Center for Fiber Preparation and Modification, Henan International Joint Laboratory of Rare Earth Composite Materials, Henan University of Engineering, Zhengzhou, Henan 451191, China. E-mail: yyp1990@haue.edu.cn*

† These authors contributed equally to this work.

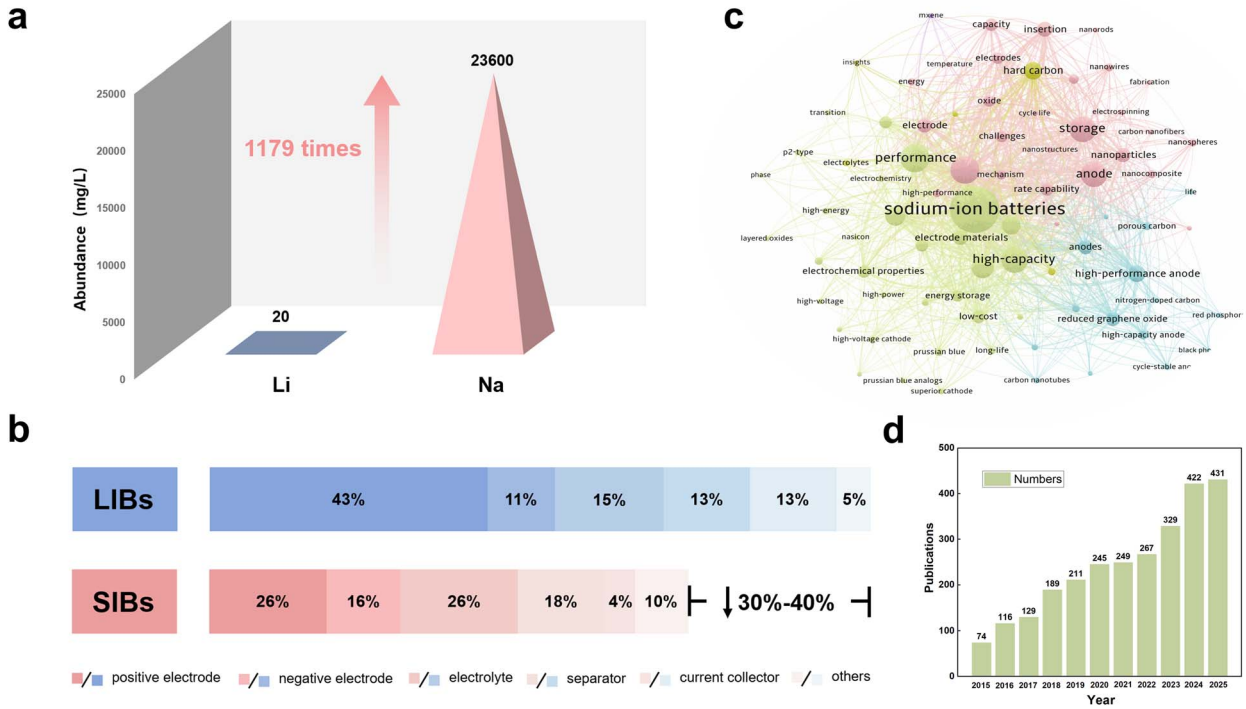

Fig. 1 (a) A comparison of the abundances of Li and Na in the Earth's crust.[2] Copyright 2022, Royal Society of Chemistry. (b) A comparison of the costs of LIBs and SIBs (the data originated from the HiNa Battery Technology Co., Ltd). (c) Research hotspots and (d) the number of publications with regard to Na_xTMO_2 cathodes (the data were collected using the Web of Science during November 2025).

For instance, the P2 phase exhibits prismatic Na^+ coordination and an ABBA stacking pattern, resulting in wide interlayer spacing that thereby facilitates Na^+ transport.[38] However, this structure typically exhibits a limited reversible capacity, which originates from its low Na content. In contrast, the O3 phase is defined by octahedral Na^+ coordination and an ABCABC oxygen stacking sequence, with three transition metal (TM) layers in a unit cell.[39,40] There is more abundant Na content and higher capacity in the O3-type structure.[41–45]

Beyond the layered phases, spinel- and tunnel-type structures have also been investigated to serve as the cathodes of SIBs. The spinel phase with a three-dimensional (3D) tunnel framework supports nearly isotropic and rapid Na^+ migration, yielding outstanding rate capability and structural robustness, albeit at the expense of limited theoretical capacity. Additionally, the tunnel-type structures, characterized by one-dimensional S-shaped channels formed by edge sharing and corner sharing of the MnO_6 octahedron, exhibit exceptional mechanical stability during cycling, resulting in long cycle life and outstanding rate capability.[46–51]

Unfortunately, Na_xTMO_2 is also affected by inadequate interfacial air stability, sluggish ion transport kinetics, and inherent structural instability (Fig. 2).[40,52–55] Studies focused on such drawbacks have been comprehensively conducted (Fig. 1c), with yearly increases in the research (Fig. 1d). The primary strategies to address these challenges include compositional regulation, surface coating, and phase engineering. Elemental doping effectively stabilizes the bulk crystal structure, while the intricate interactions between dopant and host element complicate a precise understanding of underlying mechanisms. Consequently, extensive research is required to systematically identify the optimal phase structures that yield superior electrochemical performance.[54] Currently, surface coating is performed by physically isolating the electrode from

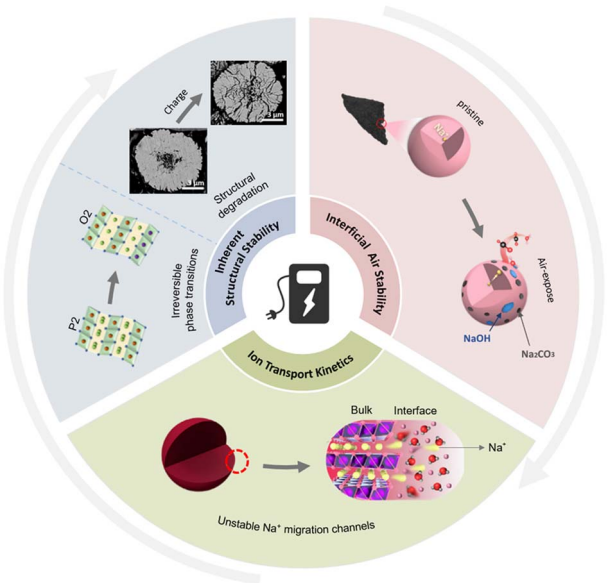

Fig. 2 The key challenges faced by Na_xTMO_2 during application.

electrolytes and air. However, it requires tedious secondary treatments.

The construction of a lattice-coherent interface in the layered lattice has been proven to be a valid method to enhance the electrochemical performance of layered oxides.[56–58] A lattice-coherent interface refers to a stable boundary formed at the atomic scale between multiple heterogeneous crystal structures through sharing lattice sequences, and is characterized by low defect density and strong bonding.[59–61] Its essential distinction from a simple physical mixture lies in the fact that the former achieves strong interactions and synergistic enhancements between phases *via* atomic-scale lattice continuity, akin to an integral mortise and tenon structure, whereas the latter involves only weak physical contacts between distinct grains, with clear phase boundaries that readily trigger performance degradation and irreversible phase transitions.[62,63] Specifically, when the lattice-coherent boundaries formed between different phase structures are used, the phase structure, interfacial integrity, and ionic transport kinetics of the bulk phase can all be reinforced (Fig. 3).[64–68] By precisely regulating the compositions or synthesis conditions, the phase composition can be tailored to promote the formation of thermodynamically stable coherent boundaries.[69–72]

The resulting coherent interfaces can effectively accommodate crystallographic strain during Na^+ (de)intercalation, inhibit the initiation and propagation of microcracks, and mitigate particle pulverization, thereby significantly improving structural strength and cycling lifespan.[73–76] Furthermore, the introduced heterogeneous phases such as spinel and tunnel configurations supply a robust and high-porosity 3D framework for ionic conduction.[77–81] To increase the interface stability, the coherent interface in the core–shell architecture is constructed as well through component regulation at the interface,[82–86] which effectively suppresses parasitic reactions and enhances the atmospheric durability.[87–89] Consequently, the construction of a coherent interface presents a pioneering design paradigm for high-performance layered cathodes. In this review, recent advances in lattice-coherent interface engineering are systematically summarized and additional insights are disscussed, so that to provide more propositions to construct high-performance Na_xTMO_2 cathodes.

2 Lattice-coherent interface in Na_xTMO_2

2.1 Enhancing phase stability

As is well known, Na_xTMO_2 generally undergoes detrimental phase transitions, which can induce severe volume changes and structural degradation, particularly under high-voltage operation.[90–92] Relying on the mutual stabilization effect between phase boundaries, an interlocked interface structure exhibits intrinsic structural stability compared to single phase materials. Xu *et al.* successfully constructed a P2/O3 biphasic $Na_{0.85}Ni_{0.34}Mn_{0.66-x}Ti_xO_2$ (x = 0, 0.11, 0.22, 0.33, and 0.44, denoted as NM, NMT_1, NMT_2, NMT_3, and NMT_4, respectively) by regulating the Ti content in the lattice.[93] This biphasic architecture combines the exceptional structural stability of the P2 phase with the high capacity of the O3 phase, with the lattice-coherent interface between them enhancing the overall structural integrity.

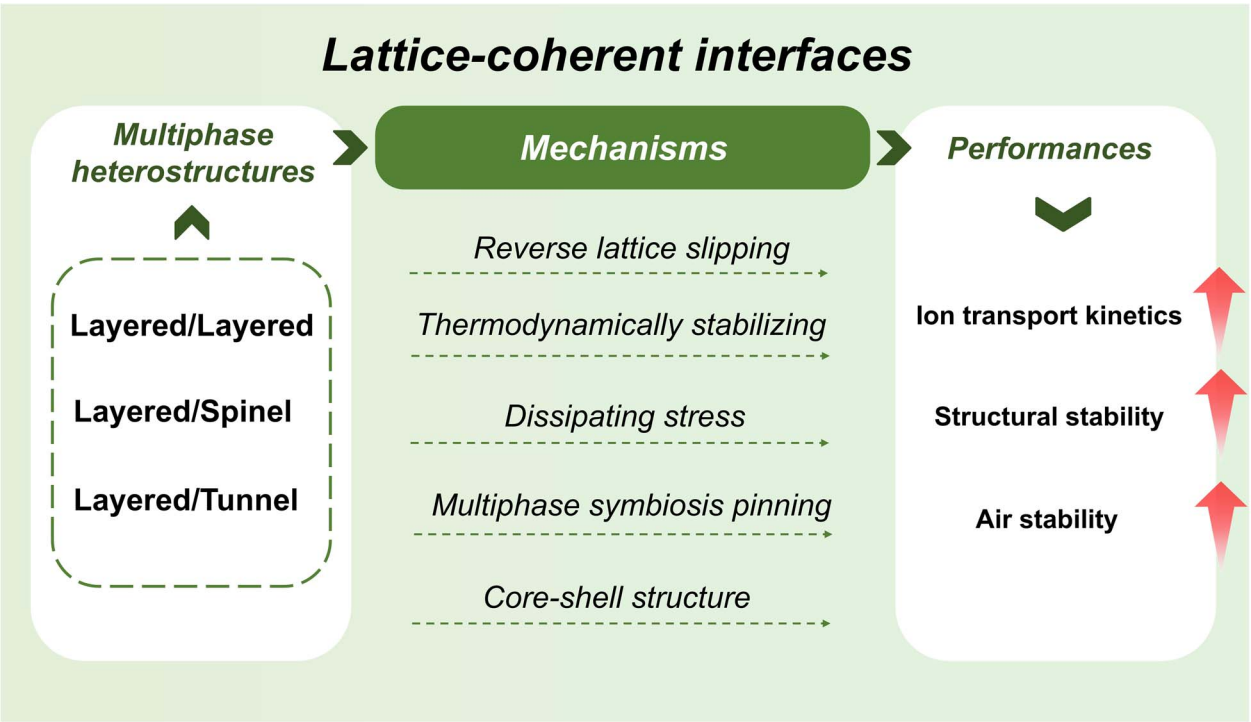

Fig. 3 A schematic representation of the performance enhancement mechanisms for the lattice-coherent interfaces in Na_xMnO_2.

The introduction of Ti substitution triggered a phase evolution from P2 to O3 during synthesis. The optimal NMT_3 was consistent with a 24.8 wt% P2 phase and 75.2 wt% O3 phase. As confirmed in Fig. 4a, a single O3 phase structure was observed at a higher Ti content ($x = 0.44$). Furthermore, *in situ* XRD analysis (Fig. 4b) demonstrated that the NMT3 cathode underwent a highly reversible phase transition of P2/O3 → P2/P3 → OP4/OP2 within a broad voltage window, effectively suppressing the detrimental P2 → O2 phase transition. The intergrown structure of the P2 and O3 phases could be regarded as a heteroepitaxial configuration, where the two phases shared polyphase boundaries. During charge and discharge within specific voltage ranges, the TMO_2 slabs in single phase may slip, while those in the adjacent phase remained stationary or slipped in the opposite direction. This opposing slippage behaviour effectively restrained layer gliding and mitigated lattice strain induced by sodium (de)intercalation.

Upon cycling, the P2 phase exhibited a volume change of 8.7% when charged to 4.4 V, whereas the O3 phase showed only a 5.7% change, which is significantly lower than the 23% observed in single phase P2-NM (Fig. 4c). Moreover, NMT_3 exhibited exceptional cycling durability, retaining 80.6% of its original capacity over 200 cycles at 1 C and delivering a reversible capacity of 82.4 mAh g^{-1} even at a high current rate of 10 C (Fig. 4d). Similarly, Zhang *et al.* developed a P2/O3 biphasic $Na_{0.732}Ni_{0.273}Mg_{0.096}Mn_{0.63}O_2$ (the actual chemical composition of P2/O3-Com_{950} 0.8 measured after synthesizing) through Mg doping, achieving precise control over the phase ratio.[94] The coexistence of the (101) plane of the O3 phase and the (004) plane of the P2 phase in high-resolution transmission electron microscopy (TEM) images (Fig. 4f) indicated the formation of a lattice-coherent interface rather than separated particles.

Fig. 4e demonstrates the superior thermodynamic stability of the P2/O3 intergrown structure, with a formation energy of −7.2 eV, which is significantly lower than those of the single P2 (−6.25 eV) and O3 (−6.43 eV) phases, and suggests that P2/O3-Com_{950} 0.8 favours a biphasic configuration. The P2/O3-Com_{950} 0.8 material also displayed highly reversible structural changes upon charge and discharge, as illustrated in Fig. 4h and i. This outstanding reversibility stemmed from the interlocking mechanism enabled by the coherent P2/O3 interface, which efficiently suppressed the interlayer gliding that was commonly encountered in single P2 or O3 structures.

As evidenced in Fig. 4g, the remarkable rate capability was captured, and was attributed to its robust structural framework. It also manifested a specific capacity of 65.9 mAh g^{-1} under a high rate of 20 C, with a capacity retention of 50.7%. This performance marks a significant enhancement over single-phase materials and other biphasic configurations with different phase ratios. Therefore, the P2/O3 biphasic structure with an atomical lattice-coherent interface is able to effectively inhibit lattice slipping and volumetric strain, and subsequently enable highly reversible structural evolution and anion redox activity.

Except for the P2/O3 interface, a lattice-coherent interface in the P2/P3 biphasic configuration is also efficient for

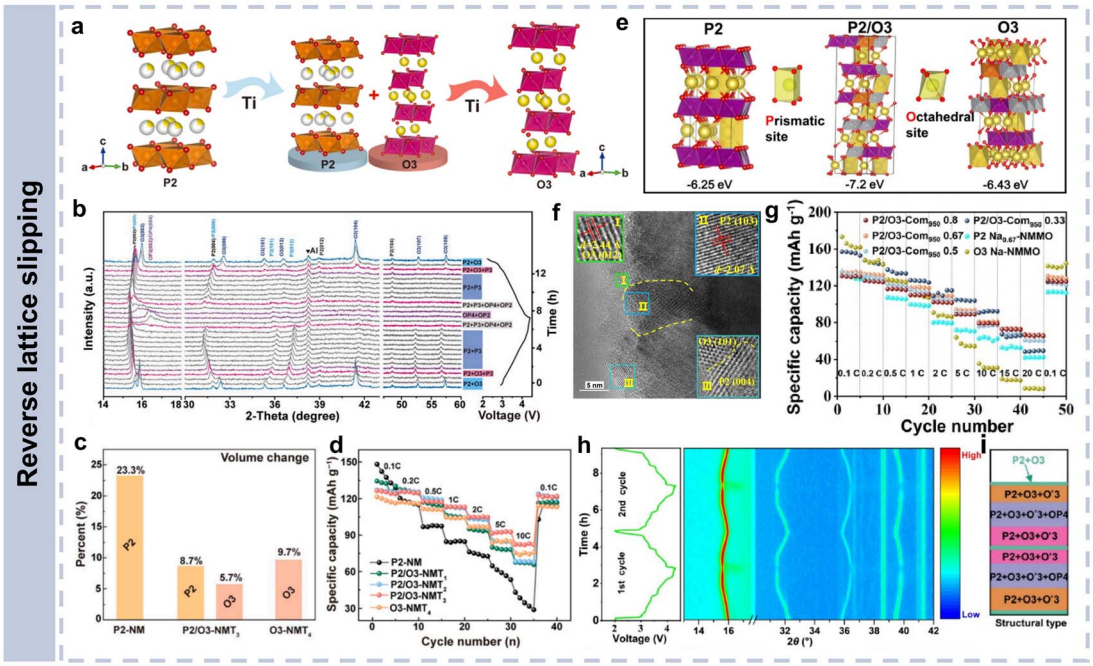

Fig. 4 (a) The phase changes in $Na_{0.85}Ni_{0.34}Mn_{0.66-x}Ti_xO_2$ as a function of Ti content. (b) Operando XRD patterns of P2/O3-NMT_3 during the first charge/discharge cycle at 0.1 C within 2.2–4.4 V. (c) The volume changes of NM, NMT_3, and NMT_4 when charged to 4.4 V. (d) Rate performances of NM, NMT_1, NMT_2, NMT_3, and NMT_4 at various current densities.[93] Copyright 2022, Elsevier. (e) Crystal structure diagrams and E_f values of P2, O3, and P2/O3 bi-phase $Na_{0.736}Ni_{0.264}Mg_{0.1}Mn_{0.636}O_2$. (f) TEM images of P2/O3-Com_{950} 0.8. (g) Rate capabilities of $Na_{0.67}Ni_{0.23}Mg_{0.1}Mn_{0.67}O_2$, $NaNi_{0.4}Mg_{0.1}Mn_{0.5}O_2$, P_2/O_3-Com_{950} 0.8, P2/O3-Com_{950} 0.67, P2/O3-Com_{950} 0.5, and P2/O3-Com_{950} 0.33. (h) *In situ* XRD patterns and corresponding charge and discharge curves (i) as well as the phase configurations of P2/O3-Com_{950} 0.8.[94] Copyright 2023, Elsevier.

strengthening the structural stability of layered bulk skeleton. Regardless of the gliding mode (P2/P3 → O2/O3 or P2/P3 → O2/O1), the formation energy of the new structures is higher than that of the original P2/P3 configuration, indicating that gliding is a thermodynamically unfavourable process.[65,95,96] Lu *et al.* successfully synthesized a well-designed P2/P3 biphasic $Na_{0.46}Mn_{0.9}Ni_{0.1}O_2$ (P2/P3-NaMNO).[65] As shown in Fig. 5a, transforming to structure 1 resulted in P2 → O2 and P3 → O3 phase transitions during desodiation, which was dictated by the oxygen-stacking sequence. However, the O3-type structure become a high-energy configuration upon desodiation, which would markedly increase the formation energy of the P2/P3 → O2/O3 transition. Conversely, sodiation-induced sliding at the phase interface produced an O2-type structure that was Na-rich, yet energetically unfavourable.

An analogous situation was observed for sliding mode 2, where the original P3 phase was transformed into the uncommon and unstable O1 phase. The inherent conflict in the preferred sliding directions of the two phases resulted in a mutual suppression of TMO_2 layer gliding within the P2/P3 composite. Consequently, as evidenced by the absence of new diffraction peaks in Fig. 5c, the material retained its original biphasic configuration over the full charge/discharge cycle, confirming its exceptional structural stability. The full-cell with an activated carbon (AC) anode delivered 81.2% capacity retention after 500 cycles (Fig. 5d), surpassing those of single-phase P2-NaMNO (67.1%) and P3-NaMNO (69.2%).

Our group synthesized a heterostructure layered phase *via* regulating the composition of tunnel type $Na_{0.44}MnO_2$ (NMO).[97] Specifically, by introducing Co into $Na_{0.44}Mn_{1-x}Co_xO_2$, the phase structure gradually transformed to the layered P2/P3 or even P3 configurations (Fig. 5e), yielding the target material $Na_{0.44}Mn_{0.7}Co_{0.3}O_2$ (NaMC-0.3). The XRD pattern of NaMC-0.3 in Fig. 5f manifested mixed hexagonal P2 and P3 phases. As shown in Fig. 5g, the morphology of NaMC-0.3 composed of micrometre-scale platelets and nanoscale granular particles, markedly differed from the rod-like shape of pristine NMO, which highlighted the role of Co substitution in driving the structural transformation.

This P2/P3 heterostructure, stabilized by mutual constraint at the coherent interface, exhibited remarkable structural reversibility. *In situ* XRD results (Fig. 5h) confirmed that upon cycling, a highly reversible phase transition sequence of P2/P3 → OP4 → P2/P3 occurred for NaMC-0.3. Collectively, these findings establish the construction of P2/P3 biphasic systems with lattice-coherent interfaces as a viable approach to improving the structural stability of layered oxide cathodes.

Beyond the interface interlocking configuration that resulted from the layered-layered biphasic structures, the hetero-structures such as P2/spinel and P2/tunnel provide an available method to construct a robust interlocking interface.[98–100] For instance, our group synthesized $Na_{0.44}Mn_{0.8}Mg_{0.2}O_2$ through Mg doping, which promoted a transition from the tunnel phase to P2 phase at high temperature, ultimately forming a P2/spinel biphasic structure within the lattice.[101] As depicted in Fig. 6a, the crystal structure of $Na_{0.44}Mn_{0.8}Mg_{0.2}O_2$ displayed two distinct atomic arrangements, corresponding to the P2 and spinel phases, and confirming the coexistence of both

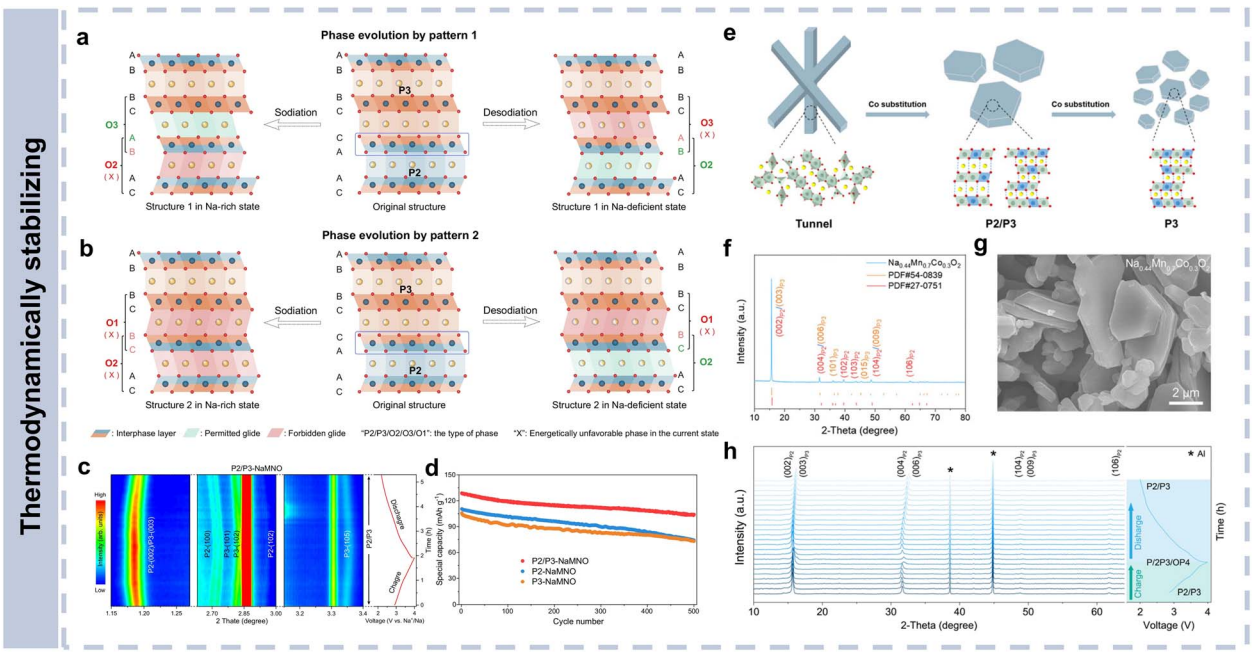

Fig. 5 Schematic diagrams of phase evolutions induced by the probable interphase gliding behaviours according to pattern (a) 1 and (b) 2. (c) Contour maps of *in situ* synchrotron XRD patterns for P2/P3-NaMNO during the first cycle. (d) Cycling performance over 500 cycles at 2 C.[65] Copyright 2025, Springer Nature. (e) A schematic diagram of the dynamic structural evolution of NMO, NaMC-0.3, and $Na_{0.44}Mn_{0.5}Co_{0.5}O_2$ with different phase structures. (f) The powder XRD pattern, (g) SEM image, and (h) *in situ* XRD patterns of NaMC-0.3.[97] Copyright 2024, Royal Society of Chemistry.

structures. Herein, the layered/spinel architecture effectively distributed mechanical stress between the two phases *via* a tightly bonded lattice-coherent interface, thereby enhancing the stability of the lattice framework.

The two-dimensional contour map in Fig. 6b and c, illustrating the von Mises stress distribution in the pristine crystal structure, revealed that the pure layered material exhibited the highest stress concentration, while the layered/spinel biphasic system showed the most uniform stress dissipation. This result theoretically verified that the spinel phase mitigated mechanical stress through the lattice-coherent interface. Furthermore, the heterostructure formed by the compatibility of cubic closely packed oxygen arrays demonstrated high mechanical strength (Fig. 6d).

The XRD results (Fig. 6e) indicated that unlike the pure P2 structure, the P2 phase in the P2/spinel composite prevented detrimental phase transitions, and the spinel phase preserved its structural integrity during cycling. These findings confirmed that the spinel phase served as a structural stabilizer to impede undesirable phase transitions through the lattice-coherent interface. Consequently, $Na_{0.44}Mn_{0.8}Mg_{0.2}O_2$ exhibited improved cycling stability, maintaining a capacity of 93 mAh g^{-1} after 500 cycles at 5 C, outperforming the pristine material (Fig. 6f).[102]

The enhanced rate performance of the products originates from the unique tunnel structure, which is known for its long-term cyclability. This structure comprises fully filled pentagonal tunnels and partially occupied S-shaped tunnels, collectively providing ample vacant sites for ion migration. P2-type materials, in contrast, face challenges such as the detrimental P2 → O2 phase transition at high voltage and Jahn–Teller distortion caused by Mn^{3+} at low voltage. Consequently, constructing a robust architecture is imperative to mitigate lattice distortion and prevent the cracking of ion diffusion pathways.

Drawing from prior work, Liu *et al.* developed a P2/tunnel biphasic $Na_{0.6}Mn_{0.93}Fe_{0.04}Mg_{0.03}O_2$ *via* a sol–gel method and subsequent calcination. This dual strategy, which integrated bulk phase modulation with crystallographic optimization, successfully established a stable lattice-coherent interface. As illustrated in Fig. 6g, such an interface was critical for enabling the synergistic interplay between layered and tunnel phases. The tunnel phase reinforced the structural stability during Na^+ insertion/extraction through this coherent interface, reducing structural degradation and lattice strain under high rates and long-term cycling.

As shown in Fig. 6h, during the initial cycle, both phases maintained structural integrity without observable P2 → O2 transition, which was commonly observed in P2-type layered oxides, corroborating the high stability of $Na_{0.6}Mn_{0.93}Fe_{0.04}Mg_{0.03}O_2$. A full cell with the $Na_{0.6}Mn_{0.93}Fe_{0.04}Mg_{0.03}O_2$ cathode and hard carbon anode retained a reversible capacity of 67.8 mAh g^{-1} after 400 cycles at 5 C, demonstrating exceptional cycling performance (Fig. 6i). Therefore, the heterostructures, such as P2/spinel and P2/tunnel, integrated *via* a lattice-coherent interface, can achieve synergistic improvements in

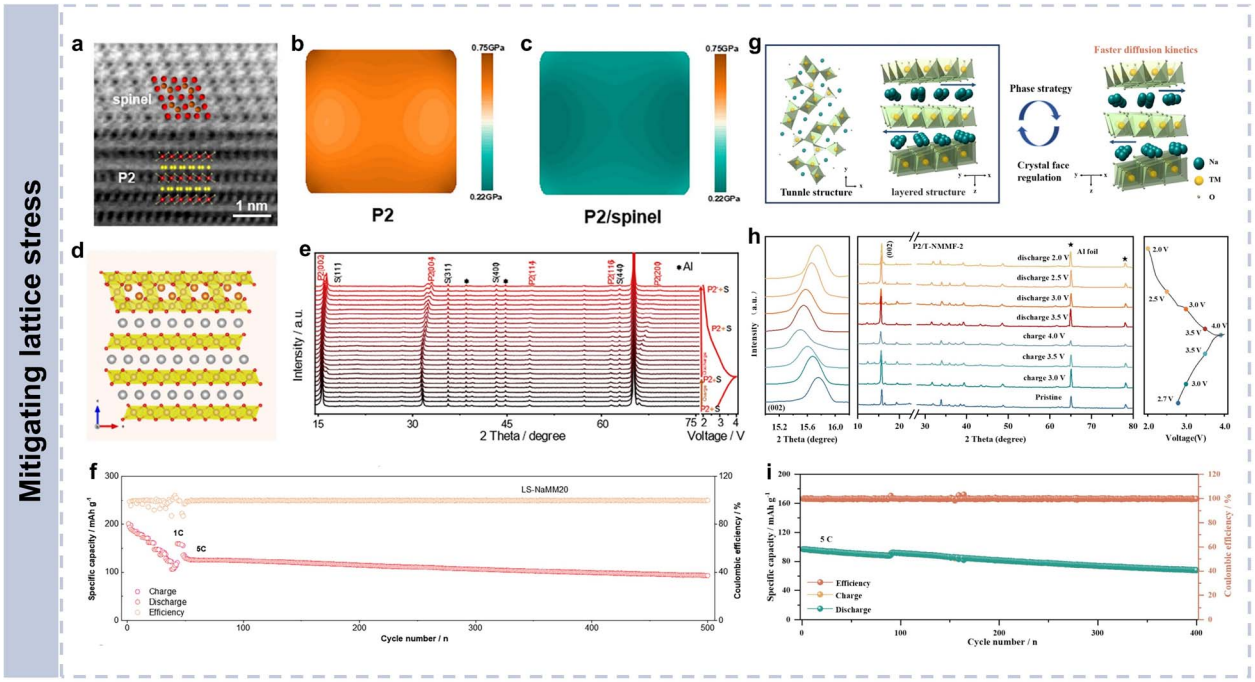

Fig. 6 (a) An ABF-STEM image of $Na_{0.44}Mn_{0.8}Mg_{0.2}O_2$. The von Mises stress of (b) P2 and (c) P2/spinel structures in the pristine state. (d) A schematic representation of the layered/spinel structure. (e) *In situ* XRD patterns of the $Na_{0.44}Mn_{0.8}Mg_{0.2}O_2$ cathode in the first cycle. (f) Cycling performance of the $Na_{0.44}Mn_{0.8}Mg_{0.2}O_2$.[101] Copyright 2025, Wiley-VCH GmbH. (g) A schematic illustration of the P2/tunnel biphasic structure. (h) *Ex situ* XRD patterns of $Na_{0.6}Mn_{0.93}Fe_{0.04}Mg_{0.03}O_2$ in the first cycle. (i) Cycle performance of $Na_{0.6}Mn_{0.93}Fe_{0.04}Mg_{0.03}O_2$ at 5 C over 400 cycles.[102] Copyright 2024, Elsevier.

mechanical stress dissipation, phase transition suppression, and ion transport.

In addition to the bi-phase interface interlocking strategy, there has been increasing interest in tri-phase heterostructures as well. Similar to biphasic intergrown configurations, the tri-phase intergrown architectures develop intricate lattice-coherent interfaces across the three phases, which facilitate multidimensional anchoring and can enhance structural integrity.[103–105] For example, for the P2/P3/spinel tri-phase interlocking $Na_{0.5}Ni_{0.05}Co_{0.15}Mn_{0.65}Mg_{0.15}O_2$ (LLS-NaNCMM15) prepared through a thermal polymerization route,[106] the modification mechanism primarily involved Mg substitution for Ni, and tailoring the local chemical environment to establish stable lattice-coherent interfaces among the three phases. This approach effectively mitigated lattice mismatch and irreversible phase transitions, thereby yielding an enhanced electrochemical performance.

As illustrated in Fig. 7a, the as-synthesized LLS-NaNCMM15 displayed a tri-phase composite structure, in which the (220) plane of the spinel phase, (002) plane of the P2 phase, and (003) plane of the P3 phase were closely interwoven, resulting in a robust interlocking configuration. Over a voltage window of 1.5–4.3 V, the material experienced only a straightforward phase transition from P2/P3/spinel to P2/P3″/spinel (Fig. 7b and c). It also exhibited minimal volumetric variation and negligible strain upon Na^+ (de)intercalation (Fig. 7d), attesting to its outstanding structural stability. These outcomes were ascribed to the strain engineering approach utilized in the tri-phase heterostructure oxide cathode.

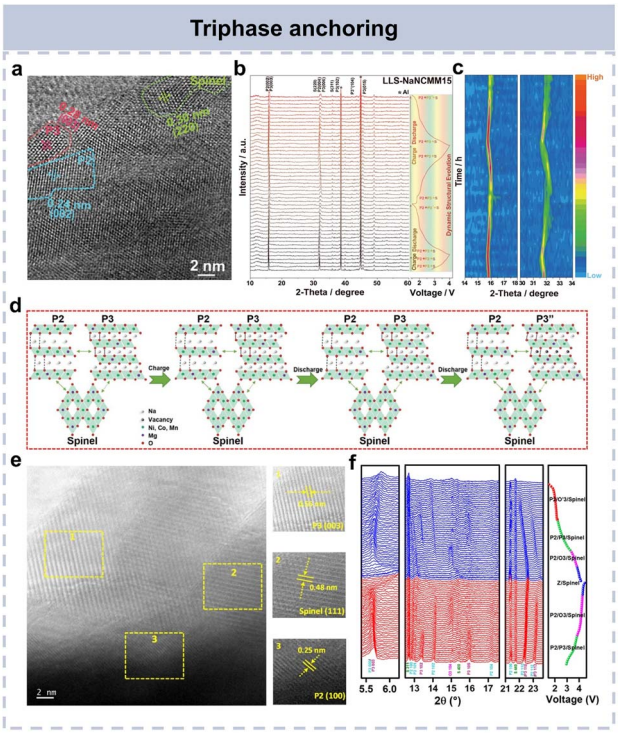

Fig. 7 (a) A HR-TEM image of P2, P3, and spinel structures. (b) *In situ* XRD patterns and (c) corresponding intensity contour maps of LLS-NaNCMM15 during the first and second charge/discharge processes at 0.1 C in the voltage range of 1.5–4.3 V. (d) A schematic illustration of the crystal structure evolution during cycling.[106] Copyright 2022, Wiley-VCH GmbH. (e) HRTEM images and (f) in operando powder diffraction patterns of Na/LS-NMNF.[107] Copyright 2022, American Chemical Society.

As reported by Bhaskar *et al.*, LS-$Na_{1/2}Mn_{2/3}Ni_{1/6}Fe_{1/6}O_2$ (LS-NMNF) with an interlocked P2/P3/spinel structure was synthesized *via* a sol–gel process assisted by citrate.[107] The P3 and spinel phases, interconnected through lattice-coherent interfaces, served as structural buffers and pinning sites to effectively inhibit slip and lattice distortion within the P2 layers during Na^+ insertion and extraction, and thus enhance the structural stability. Fig. 7e shows the coexistence configuration of P2, P3, and spinel phases in LS-NMNF, confirming successful synthesis of the tri-phase system. Throughout electrochemical cycling, the spinel phase was remained, and no detrimental P2 → P′2 phase transition signal emerged, implying excellent structural stability of the P2/P3/spinel intergrown configuration (Fig. 7f).

The existence of lattice-coherent interfaces efficiently suppressed adverse phase transformations, and nearly 100% coulombic efficiency was observed after the second cycle. Hence, the construction of tri-phase intergrown cathode materials enables mutual anchoring between heterogeneous structures, which provides structural constraints and alleviates internal stress so that irreversible phase transitions and progressive structural deterioration are suppressed.

In summary, the P2/O3, P2/P3, P2/spinel, P2/tunnel, and complex tri-phase heterostructures demonstrate the critical role of lattice-coherent interfaces in stabilizing the intrinsic structure of layered oxides. These interlocking interfaces enable mutual anchoring and constraints between heterogeneous phases, thereby effectively suppressing detrimental phase transitions, alleviating lattice strain, inhibiting interlayer gliding, and enhancing structural reversibility during cycling.

2.2 Improving ion transport kinetics

To further improve rate capability, the P2/tunnel intergrowth structure has been developed, which synergistically combines the high capacity of the layered phase with the open diffusion channels of the tunnel phase.[78,108,109] The $Na_{0.6}MnO_2$ (LT-NaMO) with a P2/tunnel biphasic intergrowth structure was synthesized *via* thermal polymerization.[110] This unique layered/tunnel configuration exhibited a lattice-coherent interface. As illustrated in Fig. 8a, the interlocking configuration was constructed by leveraging the complementary strengths of each component: the P2-type phase was characterized by its high specific capacity, while the tunnel-type structure delivered exceptional rate performance and excellent structural strength.

TEM images of LT-NaMO (Fig. 8b) show close connectivity between the layered and tunnel regions, forming efficient ion transport pathways. Relying on the lattice-coherent interface, LT-NaMO exhibited superior rate capability (Fig. 8c). Furthermore, based on the equation $i = av^b$, the b values for the oxidation peaks of LT-NaMO were all greater than 0.5, indicating that the sodium storage mechanism was primarily

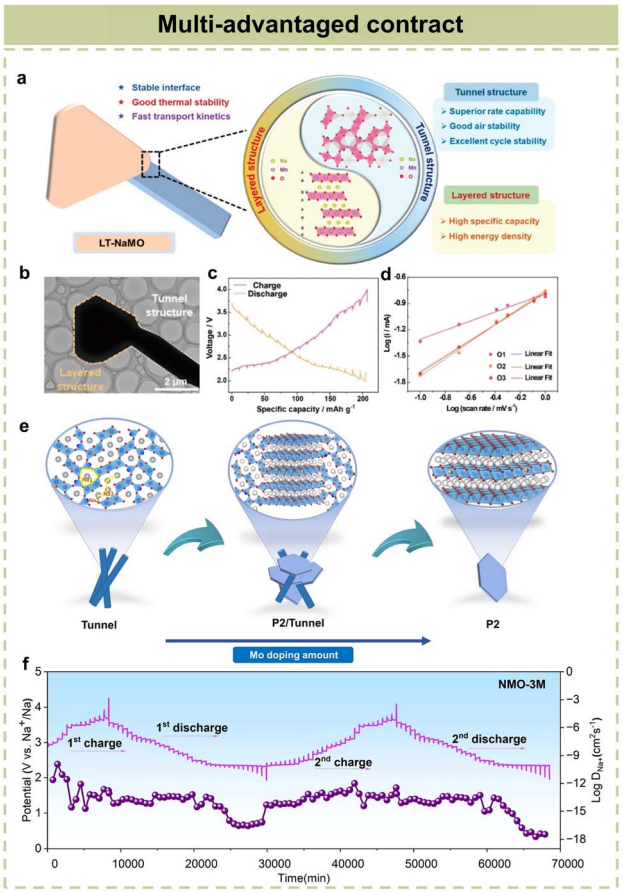

Fig. 8 (a) A schematic diagram, (b) TEM image, (c) GITT plots, and (d) log(*i*) *vs.* log(*v*) plots for $Na_{0.6}MnO_2$.[110] Copyright 2023, American Chemical Society. (e) A schematic diagram of the phase transition process for $Na_{0.44}Mn_{1-x}Mo_xO_2$ with increasing Mo content. (f) GITT curves and corresponding Na ion diffusion coefficients for NMO-3M.[111] Copyright 2024, Elsevier.

dominated by capacitive behaviour and demonstrated fast ion transport kinetics, which was consistent with its outstanding rate performance (Fig. 8d). The LT-NaMO||hard carbon full cell delivered an 85.0% capacity retention after 100 cycles, indicating promising potential for practical application.

In a different synthetic approach, trace Mo doping was used to disrupt the Mn^{3+}/Mn^{4+} charge balance in NMO, promoting a partial transition from tunnel to a P2-layered structure and resulting in a layered/tunnel interlocking architecture. Using a solid-state sintering method, they prepared Mo-doped $Na_{0.44}Mn_{1-x}Mo_xO_2$ ($x = 0$, 0.01, 0.03, and 0.05 are designated as NMO, NMO-1M, NMO-3M, and NMO-5M, respectively. Fig. 8e).[111] As shown in Fig. 8f, NMO-3M exhibited rapid desodiation/sodiation kinetics, revealing that the target material with a layered/tunnel composite structure retained the capability for fast sodium ion diffusion.

As indicated earlier, designing bi-phase systems such as P2/O3 or P2/tunnel-type successfully combines the advantages of different phases, markedly boosting the ionic transport kinetics and electrochemical behaviour of layered oxides.[112,113] Advancing from bi-phase to tri-phase structures will result in complementary advantages and weakness mitigation at a more intricate level, leading to a synergistic outcome where "1 + 1 + 1 > 3" in attributes such as ion conduction and compensating for the inherent limitations in some biphasic structures.[80,114,115] For example, the deployment of multiphase lattice-coherent interfaces allows concurrent multipath diffusion and establishes an extended lattice-coherent network, resulting in more continuous ion transport channels.

Luo *et al.* employed a targeted fluorine quenching method to produce a P2/P3/O3 tri-phase coexistence structure $Na_{0.89}Ni_{0.3}Mn_{0.55}Cu_{0.1}Ti_{0.05}O_{1.94}F_{0.06}$ (Fig. 9a), which featured a gradual O3 → P3 → P2 distribution from surface to core. The lattice-coherent interfaces among these phases provided additional Na^+ diffusion routes (Fig. 9b). The quenching treatment introduced high-density surface dislocations and defects, which facilitated dislocation motion during cycling and curtailed crack growth. Additionally, after F^- integration, the Ni content was increased. Herein, Ni ions with a larger radius and low valence as well as the introduction of robust TM-F bonds were conducive to effectively immobilize the TM ions, markedly curtailing the dislocations and convolution features, and thus stabilizing ion transport paths (Fig. 9a).[116]

Nudged elastic band (NEB) simulations confirmed a sharply decreased diffusion barrier energy for Na^+ along the octahedron → tetrahedron → octahedron route in the optimized O3 phase structure (Fig. 9c). Accordingly, the artificial dislocations and defects at coherent interfaces provide low activation energy diffusion paths *via* the dislocation pipe effect, which also facilitates ion migration and alleviates internal stress during cycling. The multiple metal–semiconductor lattice-coherent interfaces within the material (Fig. 9d) would induce internal electric fields with diverse strengths, thus increasing the electronic conductivity.

Beyond P2/P3/O3 configurations, Luo *et al.* fabricated an interlocked O3/spinel/P2 triphasic $Na_{0.98}Ni_{0.3}Cu_{0.1}Ti_{0.05}Mo_{0.05}Mn_{0.5}O_{2-\delta}S_\delta$ (NNMO-S) through an *in situ* targeted element quenching strategy.[117] The spinel phase created constrained regions between the O3 and P2 phases. Specifically, the quenching process produced numerous microcracks and defects in the inside of material particles, which propelled S^{2-} from the quenching agent to permeate into the $Na_{0.98}Ni_{0.3}Cu_{0.1}Ti_{0.05}Mo_{0.05}Mn_{0.5}O_2$ (NNMO) matrix and react with Mo^{6+}, eventually yielding a Na_2MoS_4 spinel phase (Fig. 9e).

The density functional theory (DFT) analyses indicated a markedly lower migration barrier energy along specific trajectories in NNMO-S (Fig. 9f). In this case, the spinel phase relieved the internal stress *via* lattice-coherent interfaces and then accelerated Na^+ diffusion and improved the structural durability. As confirmed by the galvanostatic intermittent titration technique (GITT) results shown in Fig. 9g, the Na^+ diffusion coefficients of NNMO-S were consistently higher than those of NNMO throughout the entire charge/discharge process. These exceptional characteristics stemmed from the distinctive O3/spinel/P2 tri-phase coherent configuration in NNMO-S.

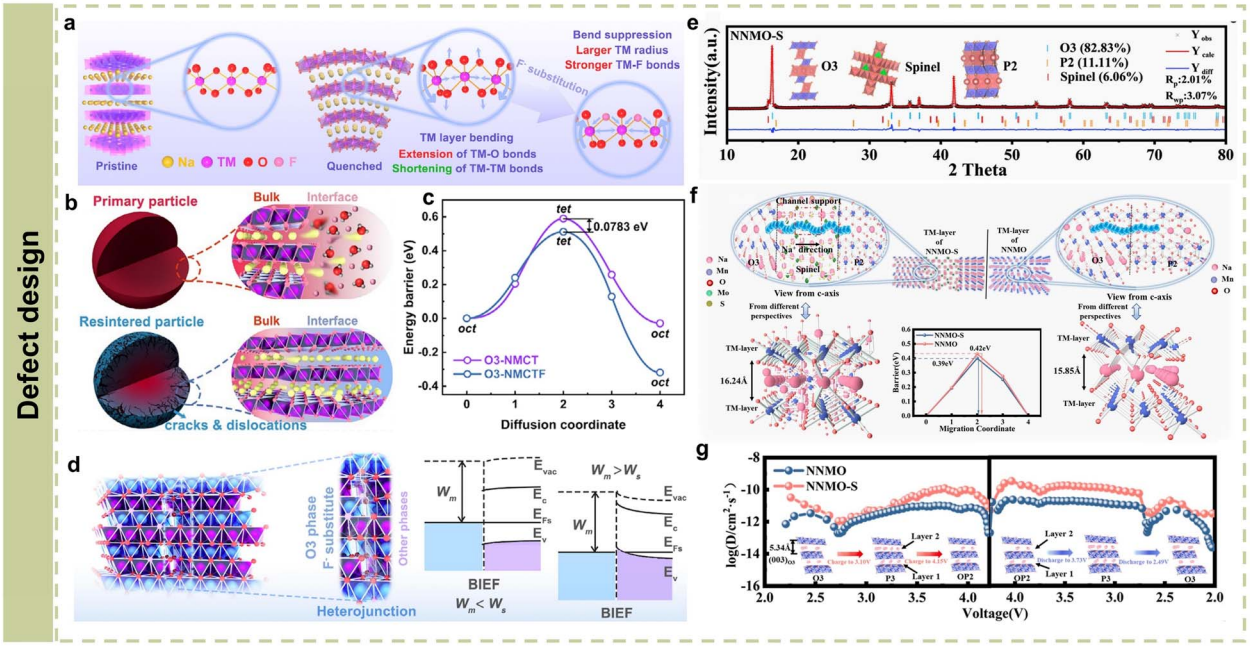

Fig. 9 (a) A schematic diagram of the structures of $Ni_{0.3}Mn_{0.55}Cu_{0.1}Ti_{0.05}$ before and after quenching. (b) Schematic illustrations of the structural enhancement mechanisms in P2/P3/O3-NMCT and P2/P3/O3-NMCTF. (c) The Na^+ diffusion barrier energies in O3-NMCT and O3-NMCTF collected using NEB calculation. (d) A schematic diagram of the built-in electric field formed between a semiconductor and a metal upon contact between different structures.[116] Copyright 2025, Wiley-VCH GmbH. (e) XRD pattern and Rietveld refinement plot and (f) the Na^+ migration roadmap in NNMO-S as well as the Na^+ migration barrier energies in NNMO-S and NNMO. (g) The GITT plots of NNMO and NNMO-S in the first cycle within 1.5–4.25 V.[117] Copyright 2025, Elsevier.

Therefore, the lattice-coherent interface is a key factor to ameliorate the ionic transport kinetics of layered phases. By establishing a coherent interface with interconnected diffusion pathways characterized by low energy barrier, rapid Na^+ migration can be achieved while maintaining configurational integrity, which will then improve the rate performance of Na_xTMO_2.

2.3 Reinforcing air stability

As to the poor surface stability of layered oxides in air, the coherent interface design would also constrict the surface side reactions resulting from H_2O and CO_2.[118–120] Liu *et al.* fabricated an O3/P2 biphasic structure $Na(Ni_{2/9}Fe_{1/3}Cu_{1/9}Mn_{1/3})_{1-x}Mn_xO_2$ (NFCM-MX) *via* gradient Mn doping. It consisted of a P2-type shell and an O3-type core, where atomic scale interlocking at the lattice-coherent interface firmly bonded the P2-type shell to the O3-type core. Such a configuration effectively shielded the material from external H_2O and CO_2 to improve its air stability. When additional Mn and Na sources were introduced, the Na and Mn atoms diffused during the heating process. Because of the slower diffusion rate of Mn relative to Na, a P2-phase shell was formed, ultimately yielding the O3/P2 biphasic structure (Fig. 10a and b).[121]

After exposure to air, the (003) peak of $NaNi_{2/9}Fe_{1/3}Cu_{1/9}Mn_{1/3}O_2$ (NFCM) exhibited a significant shift, indicating expansion and degradation of the layered structure. In contrast, the XRD patterns of $Na(Ni_{2/9}Fe_{1/3}Cu_{1/9}Mn_{1/3})_{0.98}Mn_{0.02}O_2$ (designated as NFCM-M2) remained virtually unchanged under identical conditions. This material exhibited a P2-phase proportion of 41.7% (Fig. 10c), demonstrating the exceptional stability of this biphasic structure connected *via* a lattice-coherent interface. Furthermore, NFCM-M2 delivered an optimal electrochemical performance with a capacity retention of 67.85%, dramatically higher than those of counterparts with different P2-phase proportions (Fig. 10d).

The O3/P2 biphasic NFCM-MX with an atomic scale interlocking configuration at the coherent interface was able to integrate the high-capacity O3 phase and the stable P2 phase. Compared to NFCM, the optimized NFCM-M2 exhibited superior stability due to atomic scale synergistic interlocking at the lattice-coherent interface (Fig. 10e). Furthermore, NFCM-M2 maintained its integrity even after exposure to air for a long time. Similarly, Sun *et al.* employed a wet chemical method and subsequent high-temperature calcination to construct an O3/P2 lattice-coherent interlocked configuration (Fig. 10g).[122]

Microstructural analysis confirmed the P2-$Na_{2/3}MnO_2$ (P2-NMO)-coated O3-$NaNi_{0.5}Mn_{0.5}O_2$ (O3-NNMO), as evidenced in Fig. 10f. The lattice-coherent interface enabled the protective layer to be tightly anchored to the O3 particle surface, effectively preserving the original O3 phase structure even after prolonged exposure to humid air (55% relative humidity for 3 days). The structural evolution induced by exposure was directly evidenced in the X-ray diffraction patterns by the splitting of the original O3-NNMO (003) peak. This phenomenon signified the emergence of two distinct phases: an O3 phase resulting from the

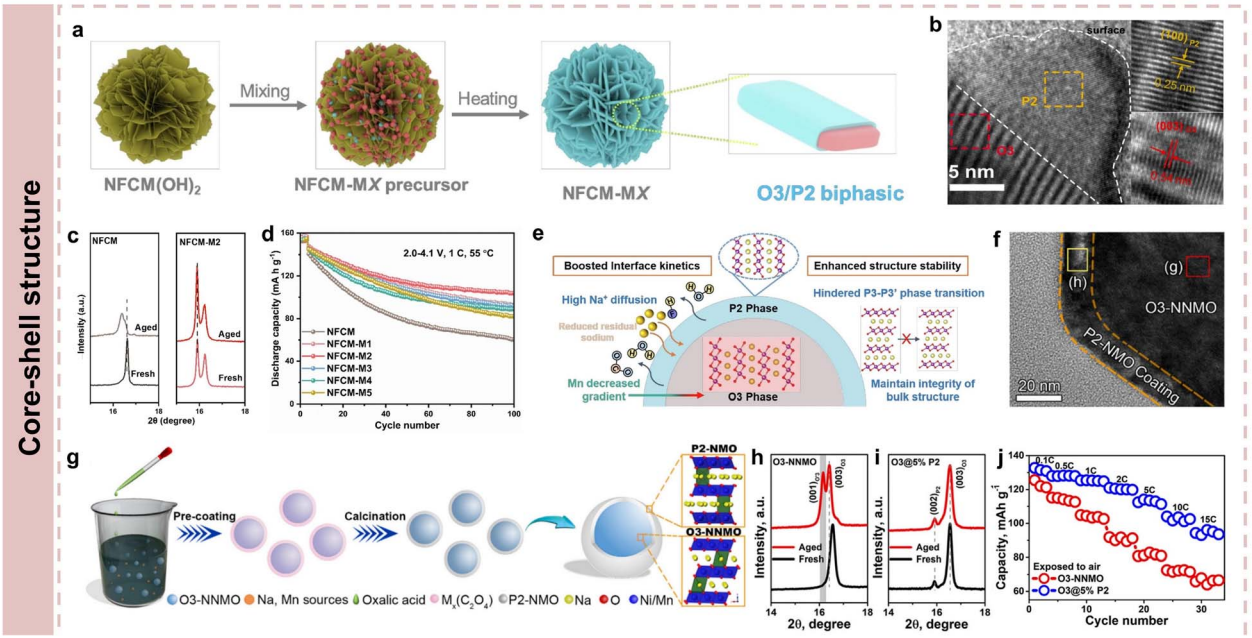

Fig. 10 (a) A schematic diagram of O3/P2-type NFCM-MX. (b) A HRTEM image of NFCM-M2. (c) XRD patterns of NFCM and NFCM-M2 after exposure to air for 3 days. (d) Cycling stability at 55 °C of NFCM and NFCM-MX. (e) A schematic diagram of the structural enhancement mechanisms for Mn-doped NCFM.[121] Copyright 2024, Elsevier. (f) A HRTEM image of O3@5% P2 heterostructure. (g) A schematic diagram of the synthesis, morphology, and crystal architecture of O3/P2-type O3@2% P2, O3@5% P2, O3@15% P2, and O3@40% P2. XRD patterns of (h) O3-NNMO and (i) O3@5% P2 after exposure to air (with a relative humidity of 55%) for 3 days. (j) The rate capability of O3-NNMO and O3@5% P2 after exposure to air.[122] Copyright 2022, Elsevier.

lattice expansion along the *c*-axis, and a distorted monoclinic O′3 phase.

This phenomenon demonstrated that a water molecule had intercalated into the interlayer (Fig. 10h). In contrast, O3@5% P2 remained unchanged under the same conditions, confirming that the lattice-coherent interface effectively maintained the structural stability of the heterogeneous cathode material (Fig. 10i). Finally, air-exposed O3@5% P2 delivered a higher capacity retention (93.8% at 0.1 C *vs.* 86.9% for O3-NNMO) (Fig. 10j). Moreover, the HC/O3@5% P2 full cell demonstrated a high-capacity retention of 80.1% after 250 cycles at a high current density of 8 C, outperforming the HC/O3-NNMO cell (75.4%). Clearly, the atomic scale interlocking at the lattice-coherent interface enabled protective heteroepitaxial growth and supplies an effective strategy for enhancing the air stability of layered oxides.

Previous studies have demonstrated that tunnel-type Na_x-MnO_2 ($x \leq 0.44$) with abundant S-channels can stabilize the phase structure, which provides sufficient space for rapid Na^+ transport and effectively mitigates lattice strain, beyond that, it also presents exceptional moisture resistance.[98,123–125] Accordingly, a bifunctional modulation strategy that simutaneously regulating the ion transfer kinetics and air satbility of layered phase by combinning with tunnel architecture had been conducted.[126] The P2/tunnel biphasic $Na_{2/3}Mn_{1-x}Ti_xO_2$ ($x = 0$, 1/9, 2/9, and 1/3, denoted as L/T-NaMT-*X* ($X = 0$, 1, 2 and 3)) were synthesized through solid-state reaction.

Fig. 11a illustrates the Ti substitution process at Mn sites, demonstrating the dynamic crystal structure evolution from layered to tunnel configuration. The L/T-NaMT-1 and L/T-NaMT-2 exhibited heterogeneous structures composed of P2-type layered and tunnel phases (Fig. 11b). Because of the lattice-coherent interface interlocking effect between layered and tunnel structures, the optimized materials achieved enhanced moisture stability that resulted from the incorporated tunnel structure (Fig. 11c).

Hydrophobicity evaluations of L-NaMT-0 and L/T-NaMT-1 (Fig. 11d and e) revealed that the water could not wet the L/T-NaMT-1 surface, showing an average contact angle of 115.13°. Whereas, L-NaMT-0 underwent complete wetting and spreading, with a contact angle of merely 61.68°. This superior moisture stability originated from lattice-coherent interface interlocking within the layered/tunnel structure, which effectively prevented water molecule intercalation and enhanced interface matching between the P2-phase and tunnel structures.[127–129]

Recently, a multifunctional interfacial modulation strategy that integrated the advantages of P2 and tunnel structures was proposed.[130] The researchers selected a typical P2-type $Na_{2/3}Ni_{1/3}Mn_{1/3}Ti_{1/3}O_2$ (NaNMT) that was characterized by poor moisture stability and severe lattice oxygen escape when it was charged to high voltages. As shown in Fig. 11f, by integrating tunnel-type NMO, the large S-channels would significantly dominate the lattice arrangement at the P2-phase interface. This interaction

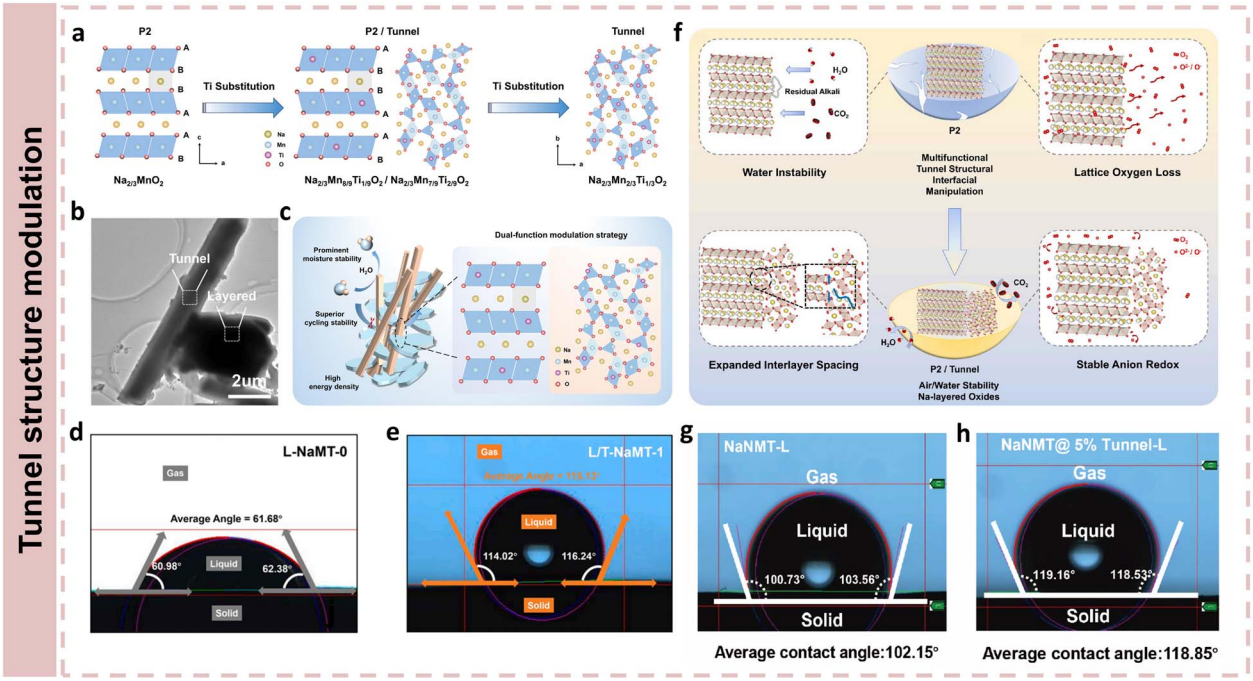

Fig. 11 (a) A schematic representation of the crystal configurations of $Na_{2/3}Mn_{1-x}Ti_xO_2$ with different Ti contents. (b) A TEM image of L/T-NaMT-1. (c) A schematic diagram of the crystal configuration of $Na_{2/3}Mn_{1-x}Ti_xO_2$ with a P2/tunnel structure. Contact angles of (d) L-NaMT-0 and (e) L/T-NaMT-1.[126] Copyright 2024, Elsevier. (f) A comparison of the crystal structures and physical/electrochemical properties for P2- and P2/tunnel-type cathodes. Average contact angles of (g) NaNMT-L and (h) NaNMT@5% Tunnel-L.[130] Copyright 2025, American Chemical Society.

was designed to induce an enlargement of the interlayer distance along the *c*-axis.

Such structural expansion effectively diminished the diffusion energy barrier of Na^+, which in turn culminated in superior fast-charging capability. Furthermore, the moderated NMO acted as a protective layer, forming an intricate interlocking structure with the internal P2 lattice. Fig. 11g and h demonstrates the excellent air/water stability of NaNMT@5% Tunnel-L (large-scale test sample of NaNMT@5% Tunnel). The average contact angle on the surface of NaNMT@5% Tunnel-L was higher (118.85°) than that of NaNMT-L (102.15°) Collectively, lattice-coherent interfaces can be used to construct effective protective barriers on the surface of layered oxide particles, significantly enhancing their air stability by suppressing moisture/CO_2 corrosion and associated side reactions. This approach provides a crucial design strategy for developing environmentally adaptable cathode materials for SIBs.

3 Summary and prospects

This review provides a systematic assessment of lattice-coherent interface engineering as an innovative approach for optimizing the structural-properties of Na_xTMO_2. This interlocked interface configuration can effectively improve the air stability of layered phases, mitigate structural degradation, and enhance ion transport kinetics.[131–133] The P2/O3 interlocked structure is the most prominent composition because it effectively alleviates lattice mismatch, suppresses high-voltage volume strain, eliminates irreversible phase transitions, and improves Na^+ diffusion efficiency, as confirmed by the works listed in Table 1.

The P2/O3 cathode materials manifest a significant improvement in capacity retention, increasing from approximately 40% to 68–81% after 200–500 cycles. For P2/P3 biphasic layered oxides, the coherent interface formed by shared TMO_2 layers induces a notable lattice contraction.[61,134–136] The layered/tunnel biphasic structure provides low barrier energy pathways for ion transport, so that to achieve high rate capability and excellent cycling stability through lattice-coherent interface. The P2/P3/O3 tri-phase layered oxide enables multipath parallel diffusion and forms an extended lattice-coherent network, thereby establishing more continuous ion transport channels.

In O3/P2 core–shell architecture, the P2 shell prevents direct contact between O3 core and electrolyte or air, significantly enhancing atmospheric stability,[137–140] which significantly enhances the cycling stability and reversibility of layered phase *via* lattice-coherent interfaces. By leveraging these multiphase intergrowth mechanisms, lattice-coherent interfaces established a universal paradigm for developing layered cathode materials with high stability, fast ion transfer kinetics, and superior environmental adaptability, greatly advancing the development of Na_xTMO_2.

The construction of lattice-coherent multiphase systems requires precise control over phase ratios and atomic coupling, which demands extreme refinement of synthesis parameters, and is a challenge that traditional trial and error methods inefficiently address.[141–144] The scalable construction of lattice-coherent interfaces is governed by thermodynamic and kinetic factors. Thermodynamically, when two phases achieve atomic-scale lattice matching, minimal lattice mismatch prominently reduces the interfacial energy, lowering the total free energy of

Table 1 The phase structures, voltage windows, phase transition behaviours, and cycling stability of the as-reported layered oxide cathodes with a lattice-coherent interface. The abbreviations "T" for tunnel and "S" for spinel are used throughout this work

Cathode material	Phase	Voltage range (V)	Phase transition	Capacity retention (pristine/modified) (%)	References
$Na_{0.85}Ni_{0.34}Mn_{0.33}Ti_{0.33}O_2$	P2/O3	2.2–4.4	P2/O3 → P2/P3 → OP4/OP2 → P2/P3 → P2/O3	40.4%/80.6% (200n, 1 C)	93
$Na_{0.732}Ni_{0.273}Mg_{0.096}Mn_{0.63}O_2$	P2/O3	2.0–4.3	P2/O3 → P2/O3/O′3 → P2/O3/O′3/OP4 → P2/O3/O′3 → P2/O3	37.2%/68.17% (500n, 5 C)	94
$Na_{0.46}Mn_{0.9}Ni_{0.1}O_2$	P2/P3	1.8–4.0	P2/P3	68.2%/81.2% (500n, 2 C)	65
$Na_{0.44}Mn_{0.7}Co_{0.3}O_2$	P2/P3	1.5–4.3	P2/P3 → OP4 → P2/P3	67.5%/84.7% (200n, 5 C)	97
$Na_{0.5}Ni_{0.05}Co_{0.15}Mn_{0.65}Mg_{0.15}O_2$	P2/P3/S	1.5–4.3	P2/P3/S → P2/P3″/S	65.6% (100n, 5 C)	106
LS-$Na_{1/2}Mn_{2/3}Ni_{1/6}Fe_{1/6}O_2$	P2/P3/S	1.5–4.0	S/P2/P3 → Sl/P2/O3 → S/Z → S/P2/O3 → S/P2/P3 → S/P2/O′3	61.0% (100n, 1 C)	107
$Na_{0.44}Mn_{0.8}Mg_{0.2}O_2$	P2/S	2.0–4.0	P2/S → P2′/S → P2/S	46.5% (500n, 5 C)	101
$Na_{0.6}Mn_{0.93}Fe_{0.04}Mg_{0.03}O_2$	P2/T	1.5–4.5	P2/T	71.5%/72.5% (1000n, 5 C)	102
$Na_{0.6}MnO_2$	P2/T	2.0–4.0	P2/T → OP4/T → P2/T	50%/70.5% (300n, 5 C)	110
$Na_{0.44}Mn_{0.97}Mo_{0.03}O$	P2/T	2.0–4.0	P2/T	77.8% (100n, 1 C)	111
$Na_{0.89}Ni_{0.3}Mn_{0.55}Cu_{0.1}Ti_{0.05}O_{1.94}F_{0.06}$	P2/P3/O3	1.5–4.5	P2/P3/O3 → P2/P3 → OP2/OP4 → P2/P3 → P2/P3/O3	66.3%/90.4% (200n, 1 C)	116
$Na_{0.98}Ni_{0.3}Cu_{0.1}Ti_{0.05}Mo_{0.05}Mn_{0.5}O_2$	O3/S/P2	1.50–4.25	O3/P2/S → O3/P3/P2/S → P3/P2/S → OP2/P2/S → P3/P2/S → O3/P3/P2/S → O3/P2/S	64.25%/86.65% (200n, 50 mA g^{-1})	117
$Na(Ni_{2/9}Fe_{1/3}Cu_{1/9}Mn_{1/3})_{0.08}Mn_{0.02}O_2$	O3/P2	2.0–4.1	O3/P2 → P3/P2 → O3/P3/P2 → O3/P2	41.54%/67.85% (100n, 1 C)	121
$NaNi_{0.5}Mn_{0.5}O_2$@5.2 mol% $Na_{2/3}MnO_2$	O3/P2	2.0–4.0	O3/P2 → O′3/P2 → P3/P2 → O3′/P2 → P3/P2 → O′3/P2 → O3/P2	74.8%/85.3% (150n, 1 C)	122
$Na_{2/3}Mn_{8/9}Ti_{1/9}O_2$	P2/T	1.5–4.3	P2/T → OP4/T → P2/T	15.2%/71.0% (300n, 1 C)	126
$Na_{2/3}Ni_{1/3}Mn_{1/3}Ti_{1/3}O_2$@5% $Na_{0.44}MnO_2$	P2/T	2.5–4.15	P2/T → OP4/T → P2/T	68.49%/80.87% (4000n, 2 C)	130

the heterostructure below that of single-phase or incoherent systems, which drives the spontaneous formation and stabilization of the interface. Kinetically, the atomic diffusion and migration rates are critical. The epitaxial nucleation of a second phase on the parent configuration can be surface-enabled by precisely controlling cooling rates or compositional gradients to facilitate the formation of a coherent interface.

Among the synthesis methods for multiphase coherent interfacial structures, thermal polymerization offers a well-defined processing route and favorable scalability, although its high-temperature processing may incur substantial energy consumption. The sol–gel approach achieves efficient replication of complex multiphase structures through molecular-level homogenization of precursors, yet faces challenges of compositional segregation and reproducibility during scale-up production.

Quenching technology serves as a critical strategy for constructing sophisticated architectures such as tri-phase intergrowth, although the rapid kinetic freezing of metastable phases may introduce lattice defects or impurity phases. Practical implementation of the syntheses methods requires comprehensive consideration of the cost, operability, and scalability limitations. The development of more precise, efficient, and stable synthesis methodologies is a primary research direction for further studies.

As shown in Fig. 12, by navigating this multi-variable design space and rapidly identifying optimal lattice-coherent interfaces, the establishment of pre-constructed databases, combined with advanced *in situ* characterization techniques and machine learning, has become indispensable.[145–147] Variable-temperature X-ray diffraction (VT-XRD) can be employed to dynamically track the phase evolution pathways during synthesis, as documented in previous studies and experiments, revealing temperature-driven phase transformation behaviours and thermodynamic stability.[148] These findings are integrated into a database for consolidated analysis. Additionally, aberration-corrected scanning transmission electron microscopy (AC-STEM) enables direct atomic-scale resolution of lattice matching, interfacial defects, and structural evolution at heterogeneous interfaces, providing direct visual evidence for understanding the formation mechanisms of coherent interfaces.[149,150]

By leveraging data acquired from such *in situ* characterization techniques, researchers are able to refine the training of machine-learning models to predict the design of multiphase structures. For instance, for P2/O3/spinel multiphase structures, the synthesis data are first retrieved from the database. The VT-XRD data reveal the specific temperatures for the formation of P2, O3, and spinel phases, while the AC-STEM data determine whether the atomically resolved interfaces obtained under specific synthesis conditions match the desired configurations. Subsequently, the database is used to train machine learning models.

Through iterative learning based on thousands of data instances, these models extract underlying patterns and establish complex mappings between composition/processing

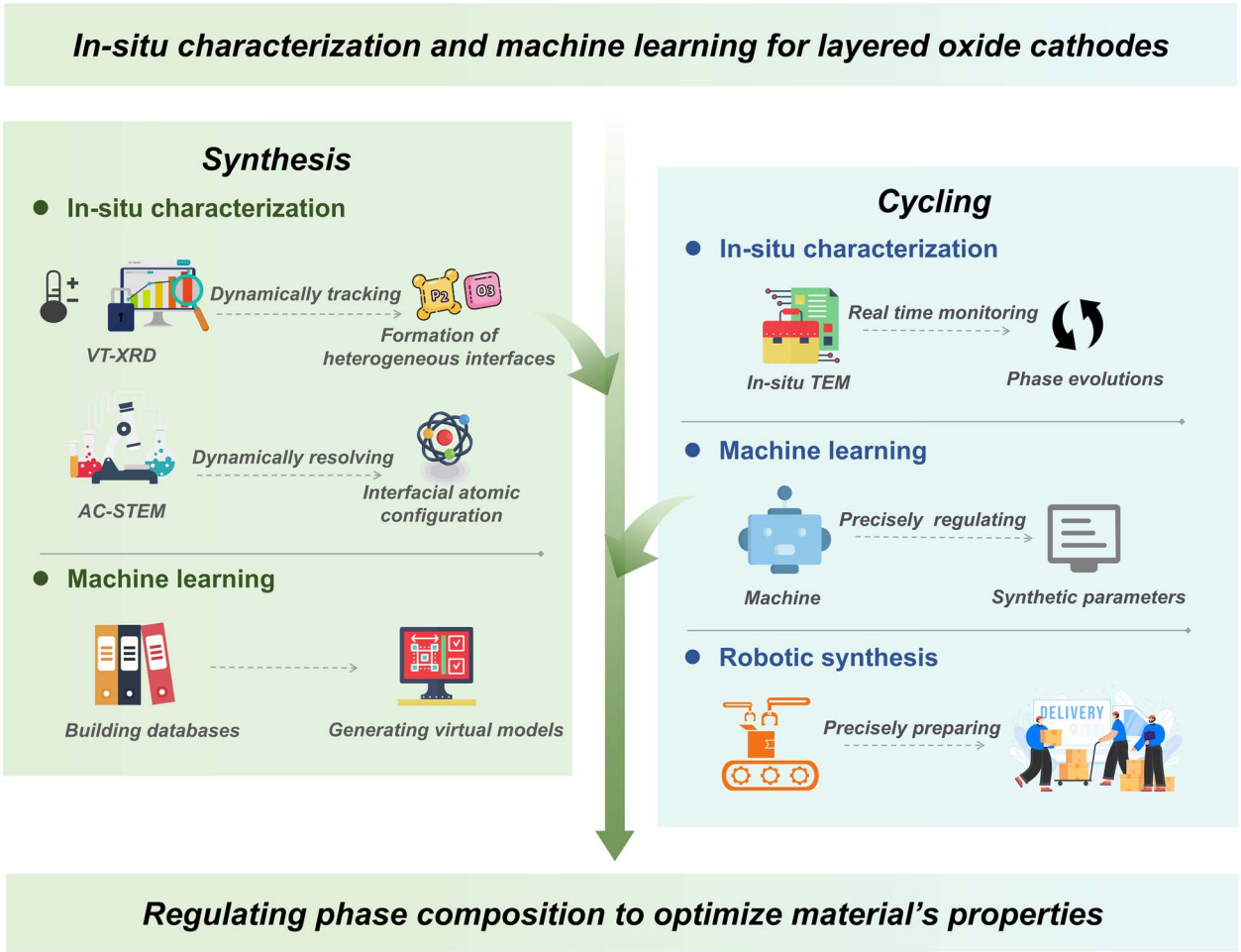

Fig. 12 The applications of characterization techniques and machine learning during the development of layered oxide cathodes with a lattice-coherent interface.

parameters and structural stability. Then, the trained models can evaluate the formation probability of various candidate combinations, effectively narrowing the exploration scope from the vast 'whole chemical space' to a focused pool of the most promising candidates. This approach enables high-throughput screening of potential interfacial configurations before committing to costly experimental efforts.[151–154]

Upon cycling, *in situ* characterization techniques and machine learning build a deeply integrated synergy. Specifically, synchrotron-based *in situ* XRD dynamically monitors phase evolution during desodiation and sodiation, providing critical kinetic feedback for machine learning models. Additionally, *in situ* TEM directly resolves the evolution of interfacial atomic arrangements throughout the cycling. These real-time characterization data are continuously fed into the machine learning models for optimization, creating a self-improving intelligent closed-loop system that enables precise control over the synthesis of multiphase heterostructures. Consequently, this intelligent closed-loop framework, which integrates characterization, simulation, and validation, replaces traditional trial and error approaches with data-driven rational design, significantly reduces the number of experimental iterations, diminishes research costs, and greatly improves the efficiency of the development of new material systems.

Currently, SIBs are regarded as a critical area in the field of energy storage.[155–157] Unlike LIBs, for which the goal is primarily high energy density, the aim with SIBs is to achieve a balanced performance profile at a moderate energy density, with cost effectiveness, safety, and a long cycle lifespan. With such a strategic position, they are suitable for unique application scenarios where reliability and economic efficiency take precedence over energy density.[158–162]

The broad market penetration of SIBs will critically depend on developing efficient material recycling protocols and building a sustainable value chain from production to full-life recovery. Innovative recycling technologies that enable the high-value regeneration of electrode materials can reduce reliance on raw materials, establish a sustainable circular model, and generate multiple economic and environmental benefits.

Author contributions

Sun-Qi Su: conceptualization, literature curation, writing–original draft. Qi-Cong Ling: conceptualization, manuscript revision. Yan-Jiang Li: methodology, manuscript revision. Ya-Ping Yan, Yan-Fang Zhu and Yao Xiao: supervision, funding acquisition.

Conflicts of interest

There are no conflicts to declare.

Data availability

No primary research results, software or code have been included and no new data were generated or analyzed as part of this review.

Acknowledgements

This work was financially supported by the National Natural Science Foundation of China (No. 22579131, 52402301, 52472240, and 52202284), the Natural Science Foundation of Zhejiang Province (LQ23E020002), and the Wenzhou Key Scientific and Technological Innovation Research Project (ZG2023053).

References

1 M.-W. Cui, Y.-L. Zhu, H. Lei, A. Liu, F.-N. Mo, K.-F. Ouyang, S. Chen, X. Lin, Z.-H. Chen, K.-K. Li, Y. Jiao, C.-Y. Zhi and Y. Huang, *Angew. Chem., Int. Ed.*, 2024, **63**, e202405428.
2 J.-Q. Wang, Y.-F. Zhu, Y. Su, J.-X. Guo, S.-Q. Chen, H.-K. Liu, S.-X. Dou, S.-L. Chou and Y. Xiao, *Chem. Soc. Rev.*, 2024, **53**, 4230–4301.
3 T. Jin, X. Ji, P.-F. Wang, K.-J. Zhu, J.-X. Zhang, L.-S. Cao, L. Chen, C.-Y. Cui, T. Deng, S.-F. Liu, N. Piao, Y.-C. Liu, C. Shen, K.-Y. Xie, L.-F. Jiao and C.-S. Wang, *Angew. Chem., Int. Ed.*, 2021, **60**, 11943–11948.
4 X.-T. Lin, S.-M. Zhang, M.-H. Yang, B.-W. Xiao, Y. Zhao, J. Luo, J.-M. Fu, C.-H. Wang, X.-N. Li, W.-H. Li, F.-P. Yang, H. Duan, J.-W. Liang, B.-L. Fu, H. Abdolvand, J.-H. Guo, G. King and X.-L. Sun, *Nat. Mater.*, 2025, **24**, 83–91.
5 X.-T. Lin, Y. Zhao, C.-H. Wang, J. Luo, J.-M. Fu, B.-W. Xiao, Y.-J. Gao, W.-H. Li, S.-M. Zhang, J.-B. Xu, F.-P. Yang, X.-G. Hao, H. Duan, Y.-P. Sun, J.-H. Guo, Y.-N. Huang and X.-L. Sun, *Angew. Chem., Int. Ed.*, 2024, **63**, e202314181.
6 Y.-J. Zeng, J. Yang, H.-Y. Yang, Y. Yang and J.-B. Zhao, *ACS Energy Lett.*, 2024, **9**, 1184–1191.
7 Z.-C. Bai, Q. Yao, M.-Y. Wang, W.-J. Meng, S.-X. Dou, H.-K. Liu and N.-N. Wang, *Adv. Energy Mater.*, 2024, **14**, 2303788.
8 X.-Y. He, Y.-H. Ling, Y.-H. Wu, Y. Lei, D.-W. Cao and C.-L. Zhang, *Small*, 2025, **21**, 2412817.
9 Y. Gao, H. Zhang, J. Peng, L. Li, Y. Xiao, L. Li, Y. Liu, Y. Qiao and S. L. Chou, *Carbon Energy*, 2024, **6**, e464.
10 Y.-C. Dou, L.-L. Zhao, Y. Liu, Z.-D. Zhang, Y.-M. Zhang, R.-F. Li, X.-Q. Liu, Y. Zhou, J.-Z. Wang and J. Wang, *Carbon Neutral.*, 2024, **3**, 954–995.
11 K. Wang, H.-X. Zhuo, J.-T. Wang, F. Poon, X.-L. Sun and B.-W. Xiao, *Adv. Funct. Mater.*, 2023, **33**, 2212607.
12 J. Peng, W. Zhang, Z. Hu, L.-F. Zhao, C. Wu, G. Peleckis, Q.-F. Gu, J.-Z. Wang, H.-K. Liu, S.-X. Dou and S.-L. Chou, *Nano Lett.*, 2022, **22**, 1302–1310.
13 W. Gu, D. He, Y.-T. Qin, C.-C. Fu, J.-H. Lu, T.-Y. Wang, G.-X. Wang and B. Sun, *Chem. Sci.*, 2025, **16**, 18050–18091.
14 H. Tian, A.-L. Song, H.-J. Tian, J. Liu, G.-J. Shao, H. Liu and G.-X. Wang, *Chem. Sci.*, 2021, **12**, 7656–7676.
15 Q.-N. Liu, Z. Hu, W.-J. Li, C. Zou, H.-L. Jin, S. Wang, S.-L. Chou and S.-X. Dou, *Energy Environ. Sci.*, 2021, **14**, 158–179.
16 B.-W. Sun, Z.-X. Sun, Y. Yang, X.-L. Huang, S.-C. Jun, C.-C. Zhao, J.-J. Xue, S.-D. Liu, H.-K. Liu and S.-X. Dou, *ACS Nano*, 2024, **18**, 28–66.
17 C. Yang, X.-W. Liu, Y. Lin, L.-M. Yin, J. Lu and Y. You, *Adv. Mater.*, 2023, **35**, 2301817.
18 J.-S. Wang, S.-S. Xin, Y. Xiao, Z.-F. Zhang, Z.-M. Li, W. Zhang, C.-J. Li, R. Bao, J. Peng, J.-H. Yi and S.-L. Chou, *Angew. Chem., Int. Ed.*, 2022, **61**, e202202518.
19 M.-L. Xu, F.-X. Zhang, Y.-H. Zhang, C. Wu, X. Zhou, X.-P. Ai and J.-F. Qian, *Chem. Sci.*, 2023, **14**, 12570–12581.
20 H.-Q. Gao, J.-J. Zeng, Z.-P. Sun, X.-F. Jiang and X.-B. Wang, *Mater. Today Energy*, 2024, **42**, 101551.
21 M.-J. Xiao and H.-Z. Sun, *J. Energy Storage*, 2025, **114**, 115824.
22 Y.-B. Niu, Y. Zhao and M.-W. Xu, *Carbon Neutral.*, 2023, **2**, 150–168.
23 T.-T. Yang, X.-Y. Wang, Z.-B. Liu and Q. Liu, *ACS Nano*, 2024, **18**, 18834–18851.
24 Y. Ouyang, Y. Zhang, G.-R. Wang, X.-F. Wei, A.-P. Zhang, J.-W. Sun, S.-Q. Wei, L. Song, F.-N. Dai and Z.-S. Wu, *Adv. Funct. Mater.*, 2024, **34**, 2401249.
25 Y.-S. Shi, E. Hu, A. Sumboja, I. T. Anggraningrum, A. Z. Syahrial and Q.-Y. Yan, *Adv. Funct. Mater.*, 2025, **35**, 2413078.
26 S. Fang, D. Bresser and S. Passerini, *Adv. Energy Mater.*, 2020, **10**, 1902485.
27 X.-C. Han, M.-M. Niu, Y. Luo, R.-L. Li, J.-D. Dan, Y.-H. Hong, X. Wu, A. V. Trukhanov, W. Ji, Y.-L. Wang, J.-H. Zhou, J.-S. Qiao, J. Zhang and X.-X. Zhao, *Nat. Synth.*, 2024, **3**, 586–594.
28 Q.-H. Shi, R.-J. Qi, X.-C. Feng, J. Wang, Y. Li, Z.-P. Yao, X. Wang, Q.-Q. Li, X.-G. Lu, J.-J. Zhang and Y.-F. Zhao, *Nat. Commun.*, 2022, **13**, 3205.
29 Q.-C. Ling, D.-C. Chen, X. Zhu, Y.-F. Zhu, Z.-Z. Hong, J. Liu, Q.-Q. Sun, Y.-B. Niu, Y. Sun, P.-F. Wang and Y. Xiao, *Adv. Mater.*, 2025, e14352.
30 Y.-H. Wan, B.-Y. Huang, W.-S. Liu, D.-L. Chao, Y.-G. Wang and W. Li, *Adv. Mater.*, 2024, **36**, 2404574.
31 J. Suo, Q.-Q. Zhao, H.-Q. Tian, L. Wang, L. Dai, J.-Y. Luo and S. Liu, *ACS Nano*, 2023, **17**, 10229–10235.

32 P.-Z. Li, T. Yuan, J. Qiu, H.-Y. Che, Q.-Q. Ma, Y.-P. Pang, Z.-F. Ma and S.-Y. Zheng, *Mater. Sci. Eng. R Rep.*, 2025, **163**, 100902.
33 G.-P. Liu, Y.-B. Mo, J.-W. Chen, Y. Peng, X. Zhu, F. Wang, X.-L. Dong and Y.-Y. Xia, *Sci. China Chem.*, 2024, **67**, 2240–2247.
34 H.-J. Shin, J.-T. Kim, A. Y. Kim, N. Noh, J. Park, C. R. Park, S. Yu, H. Kim, K. Y. Chung, J. M. Yuk, S.-T. Myung and H.-G. Jung, *Adv. Energy Mater.*, 2023, **13**, 2301220.
35 Y.-X. Kuang, Y.-X. Wu, H.-Y. Zhang and H.-P. Sun, *Molecules*, 2024, 29.
36 Y. Gupta, P. Siwatch, R. Karwasra, K. Sharma and S. K. Tripathi, *Renew. Sustain. Energy Rev.*, 2024, **192**, 114167.
37 A. Thottungal, A. Surendran, H. Enale, D. Dixon and A. Bhaskar, *J. Energy Storage*, 2025, **114**, 115808.
38 H.-Y. Hu, J.-Y. Li, Y.-F. Liu, Y.-F. Zhu, H.-W. Li, X.-B. Jia, Z.-C. Jian, H.-X. Liu, L.-Y. Kong, Z.-Q. Li, H.-H. Dong, M.-K. Zhang, L. Qiu, J.-Q. Wang, S.-Q. Chen, X.-W. Wu, X.-D. Guo and Y. Xiao, *Chem. Sci.*, 2024, **15**, 5192–5200.
39 Y.-B. Wu, H.-Y. Hu, J.-Y. Li, H.-H. Dong, Y.-F. Zhu, S.-Q. Chen, N.-N. Wang, J.-Z. Wang and Y. Xiao, *Chem. Sci.*, 2025, **16**, 3928–3937.
40 Z.-C. Jian, J.-X. Guo, Y.-F. Liu, Y.-F. Zhu, J.-Q. Wang and Y. Xiao, *Chem. Sci.*, 2024, **15**, 19698–19728.
41 L.-W. Zhang, S.-D. Huang, Y.-H. Ding and T.-B. Zeng, *RSC Adv.*, 2025, **15**, 6324–6341.
42 Y. Li, F. Wu, Y. Li, M.-Q. Liu, X. Feng, Y. Bai and C. Wu, *Chem. Soc. Rev.*, 2022, **51**, 4484–4536.
43 H. Zhang, Y. Gao, J. Peng, Y.-M. Fan, L.-F. Zhao, L. Li, Y. Xiao, W.-K. Pang, J.-Z. Wang and S.-L. Chou, *Angew. Chem., Int. Ed.*, 2023, **62**, e202303953.
44 R.-R. Li, X. Qin, X.-L. Li, J.-X. Zhu, L.-R. Zheng, Z.-T. Li and W.-D. Zhou, *Adv. Energy Mater.*, 2024, **14**, 2400127.
45 S.-N. He, R. Zhang, X. Han, Y.-F. Zhou, C. Zheng, C.-C. Li, X. Xue, Y.-J. Chen, Z.-J. Wu, J.-T. Gan, L.-N. She, F.-L. Qi, Y.-X. Liu, M.-C. Zhang, W.-B. Du, Y.-Z. Jiang, M.-X. Gao and H.-G. Pan, *Adv. Mater.*, 2025, 2413760.
46 Y.-H. Liu, Y.-H. Zhang, J. Ma, J.-W. Zhao, X. Li and G.-L. Cui, *Chem. Mater.*, 2024, **36**, 54–73.
47 K.-H. Wong, M.-W. Zhang, T.-Z. Yang, Q.-Y. Ma, S.-Q. Dai, J. Wei, G. K. Veerasubramani, A. A. AlHammadi, G. Karanikolos, E. Bekyarova, A. Elkamel and A. Yu, *Energy Storage Mater.*, 2024, **71**, 103549.
48 X.-B. Jia, J.-Q. Wang, Y.-F. Liu, Y.-F. Zhu, J.-Y. Li, Y.-J. Li, S.-L. Chou and Y. Xiao, *Adv. Mater.*, 2024, **36**, 2307938.
49 R.-M. Gao, Z.-J. Zheng, P.-F. Wang, C.-Y. Wang, H. Ye and F.-F. Cao, *Energy Storage Mater.*, 2020, **30**, 9–26.
50 J.-Y. Dai, J.-H. Li, Y. Yao, Y.-R. Wang, M.-Z. Ma, R.-L. Bai, Y.-B. Zhu, X.-H. Rui, H.-A. Wu and Y. Yu, *ACS Nano*, 2025, **19**, 11197–11209.
51 Y.-J. Han, J.-Y. Wang, Y.-H. Liu, T.-Q. Li, T.-Z. Wang, X.-Y. Li, X.-R. Ye, G.-D. Li, J.-H. Li, W.-B. Hu and Y.-D. Deng, *Carbon Neutral.*, 2024, **3**, 172–198.
52 Z.-Y. Gu, X.-X. Zhao, K. Li, J.-M. Cao, X.-T. Wang, J.-Z. Guo, H.-H. Liu, S.-H. Zheng, D.-H. Liu, H.-Y. Wu and X.-L. Wu, *Adv. Mater.*, 2024, **36**, 2400690.
53 C.-Y. Liu, K. Chen, H.-Q. Xiong, A. Zhao, H.-Y. Zhang, Q.-Y. Li, X.-P. Ai, H.-X. Yang, Y.-J. Fang and Y.-L. Cao, *eScience*, 2024, **4**, 100186.
54 Y.-F. Liu, K. Han, D.-N. Peng, L.-Y. Kong, Y. Su, H.-W. Li, H.-Y. Hu, J.-Y. Li, H.-R. Wang, Z.-Q. Fu, Q. Ma, Y.-F. Zhu, R.-R. Tang, S.-L. Chou, Y. Xiao and X.-W. Wu, *InfoMat*, 2023, **5**, e12422.
55 X.-Y. Liu, S. Li, Y.-F. Zhu, X.-Y. Zhang, Y. Su, M.-Y. Li, H.-W. Li, B.-B. Chen, Y.-F. Liu and Y. Xiao, *Adv. Funct. Mater.*, 2025, **35**, 2414130.
56 C. I. Azambou, O. O. Obiukwu, P. K. Tsobnang, I. T. Kenfack, E. E. Kalu and E. E. Oguzie, *J. Energy Storage*, 2024, **94**, 112506.
57 J.-X. Zhao, Y.-S. Meng, D.-M. Qi and F.-L. Zhu, *Ionics*, 2025, **31**, 4321–4331.
58 X.-N. Hou, C.-F. Li, M.-J. Li, Y.-S. Liu, W. Zhu, Z.-F. Li and Y.-H. Xu, *Chin. J. Chem.*, 2023, **41**, 2597–2603.
59 Q. Huang, J.-T. Liu, S. Xu, P. Wang, D. G. Ivey, B.-Y. Huang and W.-F. Wei, *Chem. Mater.*, 2018, **30**, 4728–4737.
60 Y.-J. Guo, R.-X. Jin, M. Fan, W.-P. Wang, S. Xin, L.-J. Wan and Y.-G. Guo, *Chem. Soc. Rev.*, 2024, **53**, 7828–7874.
61 R.-B. Liu, W.-Y. Huang, J. Liu, Y.-H. Li, J. Wang, Q.-S. Liu, L. Ma, G.-H. Kwon, S. N. Ehrlich, Y.-Y. Wu, T.-C. Liu, K. Amine and H.-S. Li, *Adv. Mater.*, 2024, **36**, 2401048.
62 J. Hwang, S. H. Lee, J. Kim, G. Lee, J. Park, Y. Choi, J. Lee, J. H. Lee, J. R. Choi, C.-M. Yang, I. J. Kim, B.-I. Park, S. Yang, S.-Y. Jeon, D. W. Lee and S. Yu, *Adv. Mater.*, 2025, **37**, 2502718.
63 Y.-L. An, Y. Tian, C.-L. Wei, H.-Y. Jiang, B.-J. Xi, S.-L. Xiong, J.-K. Feng and Y.-T. Qian, *ACS Nano*, 2019, **13**, 13690–13701.
64 K. Mathiyalagan, D. Shin and Y.-C. Lee, *J. Energy Chem.*, 2024, **90**, 40–57.
65 X. Zhou, C. Yang, X.-W. Liu, X. Peng, Y.-Y. Zhou, L.-G. Wang, T.-C. Liu, Y. You and J. Lu, *Nat. Commun.*, 2025, **16**, 6691.
66 D.-B. Hao, G.-Y. Zhang, D. Ning, D. Zhou, Y. Chai, J. Xu, X.-X. Yin, R.-J. Du, G. Schuck, J. Wang and Y.-L. Li, *Nano Energy*, 2024, **125**, 109562.
67 Y.-H. Shen, J. Zou, H.-H. Lan, Y.-R. Ding, Z.-J. Liang, Z.-Z. Yang, Z.-Y. Zeng, J.-C. Long, Y.-X. Zhao, L. Fu and M.-Q. Zeng, *Adv. Funct. Mater.*, 2024, **34**, 2400598.
68 L.-J. Chang, R.-F. Yang, X.-L. Bi, W. Yang, K.-D. Cai, A.-L. Wei and J. Liu, *J. Energy Storage*, 2023, **73**, 109025.
69 L.-Y. Kong, H.-X. Liu, Y.-F. Zhu, J.-Y. Li, Y. Su, H.-W. Li, H.-Y. Hu, Y.-F. Liu, M.-J. Yang, Z.-C. Jian, X.-B. Jia, S.-L. Chou and Y. Xiao, *Sci. China Chem.*, 2024, **67**, 191–213.
70 X.-L. Wang, L. Yin, A. Ronne, Y.-M. Zhang, Z.-L. Hu, S. Tan, Q.-C. Wang, B.-H. Song, M.-Y. Li, X.-H. Rong, S. Lapidus, S.-Z. Yang, E. Hu and J. Liu, *Nat. Commun.*, 2023, **14**, 7665.
71 Q. Wang, G.-H. Yu, B. Luo, W.-J. Ji, Z.-H. Liu, M.-H. Li, Y.-T. Nong, Y. Tian, X.-W. Wang, J.-F. Zhang, C.-L. Chen, C.-K. Chang, Z.-Y. Sang, Z.-W. Zhao, R.-R. Zhao and J. Liang, *ACS Nano*, 2024, **18**, 18622–18634.
72 H.-W. Li, J.-Y. Li, H.-H. Dong, Y.-F. Zhu, Y. Su, J.-Q. Wang, Y.-N. Liu, C.-Y. Wen, Z.-J. Wang, S.-Q. Chen, Z.-J. Zhang, J.-Z. Wang, Y. Jiang, S.-L. Chou and Y. Xiao, *Small*, 2024, **20**, 2306690.

73 W.-Y. Yin, Z.-X. Huang, T.-F. Zhang, T.-Q. Yang, H.-P. Ji, Y.-J. Zhou, S.-J. Shi and Y.-Q. Zhang, *Energy Storage Mater.*, 2024, **69**, 103424.
74 X.-Y. Zhang, H.-Y. Hu, X.-Y. Liu, J.-Q. Wang, Y.-F. Liu, Y.-F. Zhu, L.-Y. Kong, Z.-C. Jian, S.-L. Chou and Y. Xiao, *Nano Energy*, 2024, **128**, 109905.
75 M. Bianchini, E. Gonzalo, N. E. Drewett, N. Ortiz-Vitoriano, J. M. López del Amo, F. J. Bonilla, B. Acebedo and T. Rojo, *J. Mater. Chem. A*, 2018, **6**, 3552–3559.
76 J. H. Stansby, M. Avdeev, H. E. A. Brand, E. Gonzalo, N. E. Drewett, N. Ortiz-Vitoriano, N. Sharma and T. Rojo, *Dalton Trans.*, 2021, **50**, 1357–1365.
77 Y.-J. Li, Y.-F. Zhu, B.-B. Chen, X.-B. Jia, H.-S. Xin, G.-Z. Zhao, G. Zhu, S.-X. Dou and Y. Xiao, *Adv. Funct. Mater.*, 2025, 2504096.
78 H.-X. Liu, L.-Y. Kong, H.-R. Wang, J.-Y. Li, J.-Q. Wang, Y.-F. Zhu, H.-W. Li, Z.-C. Jian, X.-B. Jia, Y. Su, S.-L. Zhang, J.-F. Mao, S.-Q. Chen, Y. Liu, S.-L. Chou and Y. Xiao, *Adv. Mater.*, 2024, **36**, 2407994.
79 T. Zhang, J. Kong, C. Shen, S.-J. Cui, Z.-Z. Lin, Y.-Y. Deng, M.-H. Song, L.-F. Jiao, H.-T. Huang, T. Jin and K.-Y. Xie, *ACS Energy Lett.*, 2023, **8**, 4753–4761.
80 W.-L. Xu, R.-B. Dang, L. Zhou, Y. Yang, T. Lin, Q.-B. Guo, F. Xie, Z.-L. Hu, F.-X. Ding, Y.-P. Liu, Y. Liu, H.-C. Mao, J. Hong, Z.-C. Zuo, X.-Q. Wang, R. Yang, X. Jin, X.-Y. Hou, Y.-X. Lu, X.-H. Rong, N. Xu and Y.-S. Hu, *Adv. Mater.*, 2023, **35**, 2301314.
81 L. Gan, X.-G. Yuan, J.-J. Han, X. Yang, L.-T. Zheng, Z.-G. Huang and H.-R. Yao, *Adv. Funct. Mater.*, 2023, **33**, 2209026.
82 Y.-M. Zhang, D.-F. Tang, Y.-Y. Liu, J. Wang, Z.-P. Li, X. Li, G. Han, Q.-L. Wei and B.-H. Qu, *Small*, 2023, **19**, 2301141.
83 J.-X. Mu, T.-X. Cai, W.-J. Dong, C. Zhou, Z. Han and F.-Q. Huang, *Chem. Eng. J.*, 2023, **471**, 144403.
84 W. Zhao, S. Zhang, H.-H. Lai, W.-X. He, B. K. Yap, U. Feleni, X.-W. Peng, J.-L. Cui and L.-X. Zhong, *Carbon Energy*, 2025, **7**, e70047.
85 Y.-C. He, Y.-L. Huo, M.-W. Xu and Y.-R. Qi, *Adv. Funct. Mater.*, 2025, 2509099.
86 Y.-X. Chang, X.-H. Liu, Z.-Y. Xie, Z.-A. Jin, Y.-R. Guo, X. Zhang, J. Zhang, L.-R. Zheng, S. Hong, S.-L. Xu and Y.-X. Yin, *Energy Stor. Mater.*, 2025, **74**, 103972.
87 Q.-C. Ling, Q.-Q. Sun, Y.-J. Li, Z.-Z. Hong, H.-S. Xin, X.-Y. Liu, Y.-F. Zhu, S.-X. Dou and Y. Xiao, *Sci. China Chem.*, 2025, **68**, 4068–4090.
88 M.-J. Sun, Y.-J. Sun, H. Ma, S.-M. Wang, Q. Liu, G.-Q. Zhao, L.-Y. Duan, Q.-X. Hu, Q. An, K. Zeng, W.-J. Huang, X.-X. Zou, Y.-X. Yang and H. Guo, *ACS Nano*, 2025, **19**, 18386–18396.
89 W.-H. Zuo, A. Innocenti, M. Zarrabeitia, D. Bresser, Y. Yang and S. Passerini, *Acc. Chem. Res.*, 2023, **56**, 284–296.
90 Y.-Q. Wu, B.-B. Wang, Z.-X. Luo, Z.-X. Hou, B.-L. Xu, L.-J. Zhou and W.-F. Wei, *Adv. Funct. Mater.*, 2025, 2506098.
91 Q.-D. Wang, D. Zhou, C.-L. Zhao, J.-L. Wang, H. Guo, L.-G. Wang, Z.-P. Yao, D. Wong, G. Schuck, X.-D. Bai, J. Lu and M. Wagemaker, *Nat. Sustain.*, 2024, **7**, 338–347.
92 Y. You and A. Manthiram, *Adv. Energy Mater.*, 2018, **8**, 1701785.
93 L.-Z. Yu, Z.-W. Cheng, K. Xu, Y.-X. Chang, Y.-H. Feng, D. Si, M.-T. Liu, P.-F. Wang and S.-L. Xu, *Energy Storage Mater.*, 2022, **50**, 730–739.
94 L.-Y. Zhang, C.-H. Guan, J.-Q. Zheng, H.-X. Li, S.-H. Li, S.-M. Li, Y.-Q. Lai and Z.-A. Zhang, *Sci. Bull.*, 2023, **68**, 180–191.
95 K. Graff, D. Hou, E. Gabriel, J. Park, A. Koisch, R. Schrock, A. Conrado, D. Schwartz, A. Gutierrez, C. S. Johnson, E. Lee and H. Xiong, *ChemElectroChem*, 2025, **12**, e202400662.
96 X.-X. Yin, L.-T. Yang, W.-G. Zhao, Z.-Y. Hu, J. Xu, Y.-Y. Du, Z.-Q. Liu, Y. Sun, Y.-H. Deng, J. Wang, P. Adelhelm, R. Si and D. Zhou, *Adv. Energy Mater.*, 2025, 2406184.
97 Y.-F. Liu, H.-Y. Hu, Y.-F. Zhu, D.-N. Peng, J.-Y. Li, Y.-J. Li, Y. Su, R.-R. Tang, S.-L. Chou and Y. Xiao, *Chem. Commun.*, 2024, **60**, 6496–6499.
98 Y. Xiao, Y.-F. Liu, H.-W. Li, J.-Y. Li, J.-Q. Wang, H.-Y. Hu, Y. Su, Z.-C. Jian, H.-R. Yao, S.-Q. Chen, X.-X. Zeng, X.-W. Wu, J.-Z. Wang, Y.-F. Zhu, S.-X. Dou and S.-L. Chou, *InfoMat*, 2023, **5**, e12475.
99 Z.-Q. Li, Y.-F. Liu, H.-X. Liu, Y.-F. Zhu, J.-Q. Wang, M.-K. Zhang, L. Qiu, X.-D. Guo, S.-L. Chou and Y. Xiao, *Chem. Sci.*, 2024, **15**, 11302–11310.
100 Q. Pang, M.-K. Zhang, Y. Song, Y.-Y. Liu, M.-Q. Tang, S.-Q. Su, L. Qiu, Y. Xiao and X.-D. Guo, *Chem. Sci.*, 2025, **16**, 4237–4244.
101 Y. Xiao, Q.-Q. Sun, D.-C. Chen, J.-Q. Wang, J.-J. Ding, P. Tan, Y. Sun, S.-L. Zhang, P.-F. Wang, J.-F. Mao and Y.-F. Zhu, *Adv. Mater.*, 2025, **37**, 2504312.
102 Y.-C. Zhou, M.-W. Pang, M.-J. Zhang, Y.-L. Yuan, Y.-Y. Yang, F.-L. Qin, W.-F. Liu, T. Chen and K.-Y. Liu, *Chem. Eng. J.*, 2024, **501**, 157527.
103 R.-R. Li, J. Gao, J.-P. Li, H. Huang, X.-L. Li, W.-L. Wang, L.-R. Zheng, S.-M. Hao, J.-S. Qiu and W.-D. Zhou, *Adv. Funct. Mater.*, 2022, **32**, 2205661.
104 Y.-R. Yang, W. Zhang, Y.-J. Zhang, S.-T. Sun, W. Wang, S. Jin, C. Liu, T.-N. Lin, X.-Y. Xu, Z.-X. Liu, H. Huo, M. Chen, J.-L. Wang, R.-H. Li and C.-S. Dai, *J. Energy Chem.*, 2025, **110**, 176–185.
105 Z.-B. Zhao, G. Sun, Y.-M. Zhang, R. Hua, X.-T. Wang, N.-T. Wu, J. Li, G.-L. Liu, D.-L. Guo, A. Cao, X.-M. Liu and H.-S. Hou, *Adv. Funct. Mater.*, 2024, **34**, 2314679.
106 H.-Y. Hu, Y.-F. Zhu, Y. Xiao, S. Li, J.-Y. Li, Z.-Q. Hao, J.-H. Zhao and S.-L. Chou, *Adv. Energy Mater.*, 2022, **12**, 2201511.
107 A. Thottungal, A. Sriramajeyam, A. Surendran, H. Enale, A. Sarapulova, O. Dolotko, Q. Fu, M. Knapp, D. Dixon and A. Bhaskar, *ACS Appl. Mater. Interfaces*, 2024, **16**, 27254–27267.
108 Z.-C. Jian, W.-J. Shi, Y.-F. Liu, X.-Y. Li, J.-Y. Li, Y.-F. Zhu, X. Zhu, Y.-C. Li, P. Tan, P.-F. Wang, S.-Q. Chen, S.-L. Zhang, J.-F. Mao, G.-M. Zhou, X.-D. Guo, J.-Z. Wang, S.-X. Dou and Y. Xiao, *Energy Environ. Sci.*, 2025, **18**, 7995–8008.
109 J.-Y. Li, H.-Y. Hu, H.-W. Li, Y.-F. Liu, Y. Su, X.-B. Jia, L.-F. Zhao, Y.-M. Fan, Q.-F. Gu, H. Zhang, W.-K. Pang, Y.-F. Zhu, J.-Z. Wang, S.-X. Dou, S.-L. Chou and Y. Xiao, *ACS Nano*, 2024, **18**, 12945–12956.

110 Y. Su, N.-N. Zhang, J. Y. Li, Y.-f. Liu, H.-Y. Hu, J.-Q. Wang, H.-W. Li, L.-Y. Kong, X.-B. Jia, Y.-F. Zhu, S.-Q. Chen, J.-Z. Wang, S.-X. Dou, S.-l. Chou and Y. Xiao, *ACS Appl. Mater. Interfaces*, 2023, **15**, 44839–44847.
111 J.-Q. Wang, Q.-Q. Sun, J. Yu, J.-X. Guo, N.-K. Mo, H.-W. Li, Y. Su, S.-Q. Zhao, Y.-F. Zhu, H.-B. Chu, S.-X. Dou and Y. Xiao, *Composites, Part B*, 2024, 284.
112 J.-Y. Li, H.-Y. Hu, J.-Z. Wang and Y. Xiao, *Carbon Neutral.*, 2022, **1**, 96–116.
113 Y. Xiao, H. R. Wang, H. Y. Hu, Y. F. Zhu, S. Li, J. Y. Li, X. W. Wu and S. L. Chou, *Adv. Mater.*, 2022, **34**, 2202695.
114 D.-R. Yang, Y.-T. Long, X.-W. Gao, Z.-W. Zhao, H. Chen, Q.-S. Lai, C. Li, R.-Z. Niu, Z.-M. Liu, Q.-F. Gu and W.-B. Luo, *Adv. Energy Mater.*, 2025, **15**, 2404999.
115 T. Chen, C.-Y. Wen, C. Wu, L. Qiu, Z.-G. Wu, J.-Y. Li, Y.-F. Zhu, H.-Y. Li, Q.-Q. Kong, Y. Song, F. Wan, M.-Z. Chen, I. Saadoune, B.-H. Zhong, S.-X. Dou, Y. Xiao and X.-D. Guo, *Chem. Sci.*, 2023, **14**, 13924–13933.
116 D.-R. Yang, C. Liu, X.-W. Gao, Z.-W. Zhao, Q.-F. Gu, Y.-T. Long, Q.-S. Lai, H. Chen, Z.-M. Liu and W.-B. Luo, *Angew. Chem., Int. Ed.*, 2025, **64**, e202500939.
117 Z. Nie, C. Liu, Q.-S. Lai, W. Li, Q. Li, R. Yang, X.-W. Gao, Q.-F. Gu and W.-B. Luo, *Energy Stor. Mater.*, 2025, **74**, 103971.
118 Z.-Q. Li, L.-Y. Zhang, X.-L. Ge, C.-X. Li, S.-H. Dong, C.-X. Wang and L.-W. Yin, *Nano Energy*, 2017, **32**, 494–502.
119 Y.-D. Guo, J.-C. Jiang, J. Xie, X. Wang, J.-Z. Li, D.-H. Wang and A.-J. Zhou, *Rare Met.*, 2022, **41**, 3740–3751.
120 Z.-C. Yan, L. Liu, J.-L. Tan, Q. Zhou, Z.-F. Huang, D.-D. Xia, H.-B. Shu, X.-K. Yang and X.-Y. Wang, *J. Power Sources*, 2014, **269**, 37–45.
121 W.-B. Wu, P. Zhang, S.-Q. Chen, X.-H. Liu, G.-L. Feng, M.-H. Zuo, W.-Y. Xing, B. Zhang, W.-F. Fan, H. Zhang, P. Zhang, J. Zhang and W. Xiang, *J. Colloid Interface Sci.*, 2024, **674**, 1–8.
122 X.-H. Liang, T.-Y. Yu, H.-H. Ryu and Y.-K. Sun, *Energy Storage Mater.*, 2022, **47**, 515–525.
123 X. He, J. Wang, B. Qiu, E. Paillard, C. Ma, X. Cao, H.-D. Liu, M. C. Stan, H.-D. Liu, T. Gallash, Y. S. Meng and J. Li, *Nano Energy*, 2016, **27**, 602–610.
124 Y.-F. Liu, H.-Y. Hu, J.-Y. Li, H.-R. Wang, Y. Zhao, J.-Q. Wang, Y.-B. Wu, Y.-J. Li, G.-Y. Zhang, Q.-Q. Sun, Y.-F. Zhu, R.-R. Tang, X.-W. Wu, J.-Z. Wang, S.-X. Dou, S.-L. Chou and Y. Xiao, *Sci. China Chem.*, 2024, **67**, 4242–4250.
125 Z.-Q. Chen, S.-W. Kang, J.-M. Peng, Y.-J. Cai, Y.-G. Huang, Q.-C. Pan, F.-H. Zheng, H.-Q. Wang, Q.-Y. Li and S.-J. Hu, *ACS Energy Lett.*, 2023, **8**, 417–419.
126 Z.-C. Jian, Y.-F. Liu, Y.-F. Zhu, J.-Y. Li, H.-Y. Hu, J.-Q. Wang, L.-Y. Kong, X.-B. Jia, H.-X. Liu, J.-X. Guo, M.-Y. Li, Y.-S. Xu, J.-F. Mao, S.-L. Zhang, Y. Su, S.-X. Dou, S.-L. Chou and Y. Xiao, *Nano Energy*, 2024, **125**, 109528.
127 X. Wang, P. Sun, S.-T. Yuan, L. Yue and Y.-F. Zhao, *Chin. Chem. Lett.*, 2025, **36**, 110015.
128 Y.-C. Huang, S. Gu, X. Xu, Z.-B. An, X.-D. Han, Y.-L. Cao, D.-S. He, F.-C. Zhang, H. Guo, Y. Liu, X.-Q. Liao, G.-Y. Liu, P.-W. Liu, F. Wu, Y.-Z. Li, Z.-Y. Wang, Z.-Q. Wang, C. Ding, Y.-F. Wang, J.-J. Chen, M.-Y. Yang, F. Jiang, Y.-H. Deng, Z.-H. Xu and Z.-G. Lu, *Adv. Mater.*, 2025, **37**, 2408012.
129 J. Liu, W.-Y. Huang, R.-B. Liu, J. Lang, Y.-H. Li, T.-C. Liu, K. Amine and H.-S. Li, *Adv. Funct. Mater.*, 2024, **34**, 2315437.
130 X.-Y. Zhang, L.-Y. Kong, J.-J. Ding, Y.-F. Zhu, J.-Y. Li, Z.-C. Jian, H.-S. Xin, M.-Y. Li, P. Tan, W.-K. Pang, S.-X. Dou and Y. Xiao, *ACS Energy Lett.*, 2025, **10**, 2858–2867.
131 E. Gabriel, P. Wang, K. Graff, S. D. Kelly, C.-J. Sun, C.-J. Deng, I. Hwang, J. Liu, C. Li, S. Kuraitis, J. Park, E. Lee, A. Conrado, J. Pipkin, M. Cook, S. McCallum, Y.-Y. Xie, Z.-H. Chen, K. M. Wiaderek, A. Yakovenko, Y. Ren, Y.-M. Xiao, Y. Liu, E. Graugnard, Y.-Y. Hu, D.-W. Hou and H. Xiong, *Nano Energy*, 2025, **134**, 110556.
132 M.-J. Tang, J. Yang, H. Liu, X.-Y. Chen, L. Kong, Z.-W. Xu, J.-F. Huang and Y.-Y. Xia, *ACS Appl. Mater. Interfaces*, 2020, **12**, 45997–46004.
133 E. Lee, J. Lu, Y. Ren, X.-Y. Luo, X.-Y. Zhang, J.-G. Wen, D. Miller, A. DeWahl, S. Hackney, B. Key, D.-H. Kim, M. D. Slater and C. S. Johnson, *Adv. Energy Mater.*, 2014, **4**, 1400458.
134 H.-L. Ren, X.-W. Gao, D.-R. Yong, Z.-M. Liu, X.-C. Wang, G.-P. Gao, H. Chen, Q.-F. Gu and W.-B. Luo, *Chem.–Eng. J.*, 2024, **494**, 152787.
135 T. Park, J. Kim, Y. Jung, J. Sun and K. Min, *J. Energy Chem.*, 2025, **107**, 103–113.
136 C. Wang, H. Long, L.-J. Zhou, C. Shen, W. Tang, X.-D. Wang, B.-B. Tian, L. Shao, Z.-Y. Tian, H.-J. Su and K.-Y. Xie, *J. Mater. Sci. Technol.*, 2021, **66**, 121–127.
137 H.-R. Yao, L.-T. Zheng, S. Xin and Y.-G. Guo, *Sci. China Chem.*, 2022, **65**, 1076–1087.
138 B.-X. Ouyang, T. Chen, X.-C. Liu, M.-J. Zhang, P.-G. Liu, P.-L. Li, W.-F. Liu and K.-Y. Liu, *Chem.–Eng. J.*, 2023, **458**, 141384.
139 Y.-B. Hong, H.-B. Lin, X.-B. Ye, L.-Y. Zhang, Y.-M. Zhang, H.-R. Yao, L.-T. Zheng, Y.-Y. Huang, Z.-G. Huang and Z.-S. Hong, *Energy Stor. Mater.*, 2025, **77**, 104188.
140 Z. Chen, Y.-N. Wu, Q. Yang, T.-T. Huang, S. Li, S. Shi, Y. Zhang, M.-M. Fan, T.-T. Huo, X.-J. Bai, G.-L. Yu, M.-Y. Li, W. Zhang, X.-Z. Zhou, L. Li, K.-X. Lei, S.-X. Dou and S.-J. Zheng, *Nano Res.*, 2025, **18**, 94907607.
141 A. Sengupta, A. Kumar, A. Bano, A. Ahuja, H. Lohani, S. H. Akella, P. Kumari, M. Noked, D. T. Major and S. Mitra, *Energy Storage Mater.*, 2024, **69**, 103435.
142 I. Lee, G. Oh, S. Lee, T.-Y. Yu, M. H. Alfaruqi, V. Mathew, B. Sambandam, Y.-K. Sun, J.-Y. Hwang and J. Kim, *Energy Storage Mater.*, 2021, **41**, 183–195.
143 C.-Q. Ren, Y.-L. Dong and Y. Lei, *Small*, 2025, 2501262.
144 Z.-Z. Hong, Z.-C. Jian, Y.-F. Zhu, Y.-J. Li, Q.-C. Ling, H.-S. Xin, D.-D. Wang, C. Wu and Y. Xiao, *Chem. Sci.*, 2025, **16**, 17058–17085.
145 T.-X. Cai, A. Chen, S. Liang, J.-X. Mu, L.-L. Wang, W. He, K.-H. Tao, J.-J. Li and F.-Q. Huang, *Adv. Mater.*, 2025, e08717.
146 B. Oral, B. Tekin, D. Eroglu and R. Yildirim, *J. Power Sources*, 2022, **549**, 232126.
147 M. Kim, W.-H. Yeo and K. Min, *Energy Storage Mater.*, 2024, **69**, 103405.

148 A. R. Genreith-Schriever, A. Alexiu, G. S. Phillips, C. S. Coates, L. A. V. Nagle-Cocco, J. D. Bocarsly, F. N. Sayed, S. E. Dutton and C. P. Grey, *Chem. Mater.*, 2024, **36**, 2289–2303.
149 Q. Li, H. Qian, T.-Y. Zheng, X.-Y. Sun, Y.-F. Liu and Y.-N. Lyu, *J. Alloys Compd.*, 2022, **922**, 166210.
150 Z.-Y. Dong and Y.-H. Ma, *Nat. Commun.*, 2020, **11**, 1588.
151 Y.-F. Huang, W.-J. Zhang, Y.-F. Zhou, Y.-Q. Wang, L.-S. Li, H. Shao, X.-R. Li, Z.-J. Hong, H. Xia, Y.-B. Shen and L.-W. Chen, *ACS Nano*, 2024, **18**, 13106–13116.
152 H. Rostami, J. Valio, P. Suominen, P. Tynjälä and U. Lassi, *Chem. Eng. J.*, 2024, **495**, 153471.
153 S.-T. Xu, H.-T. Dong, D. Yang, C. Wu, Y. Yao, X.-H. Rui, S.-L. Chou and Y. Yu, *ACS Cent. Sci.*, 2023, **9**, 2012–2035.
154 C.-C. Wang, L.-J. Liu, S. Zhao, Y.-C. Liu, Y.-B. Yang, H.-J. Yu, S. Lee, G.-H. Lee, Y.-M. Kang, R. Liu, F.-J. Li and J. Chen, *Nat. Commun.*, 2021, **12**, 2256.
155 D. Wang, Y.-P. Deng, Y.-H. Liu, Y. Jiang, B.-H. Zhong, Z.-G. Wu, X.-D. Guo and Z.-W. Chen, *Nano Energy*, 2023, **110**, 108340.
156 L.-Z. Wang, Q.-M. Li, Z.-Y. Chen, Y.-T. Wang, Y.-F. Li, J.-L. Chai, N. Han, B. Tang, Y.-C. Rui and L. Jiang, *Small*, 2024, **20**, 2310426.
157 Y.-J. Wu, W. Shuang, Y. Wang, F.-Y. Chen, S.-B. Tang, X.-L. Wu, Z.-Y. Bai, L. Yang and J.-J. Zhang, *Electrochem. Energy Rev.*, 2024, **7**, 17.
158 B. Liu, T.-F. Song, L. Chen, A. T. Shekhar, M. Mirolo, V. Vinci, J. Drnec, J. Cornelio, D. Xie, E. H. Driscoll, P. R. Slater and E. Kendrick, *Adv. Energy Mater.*, 2025, 2405894.
159 T. Chen, B.-X. Ouyang, X.-W. Fan, W.-L. Zhou, W.-F. Liu and K.-Y. Liu, *Carbon Energy*, 2022, **4**, 170–199.
160 Y.-H. Wu, Z.-Q. Zhao, X.-R. Hao, R. Xu, L.-S. Li, D. Lv, X.-L. Huang, Q. Zhao, Y. Xu and Y.-S. Wu, *Carbon Neutral.*, 2023, **2**, 551–573.
161 H.-W. Li, J.-Q. Wang, J. Yu, J.-Y. Li, Y.-F. Zhu, H.-H. Dong, Z.-J. Zhang, Y. Jiang, S.-X. Dou and Y. Xiao, *Chem. Sci.*, 2025, **16**, 9679–9690.
162 H.-Y. Hu, Y.-C. Li, Y.-F. Zhu, H.-D. Liu, W. Xiang, J.-Z. Wang and Y. Xiao, *Chem. Sci.*, 2025, **16**, 15714–15722.